



Wacey, D. (2016). Advanced analytical techniques for studying the morphology and chemistry of Proterozoic microfossils. In *Earth System Evolution and Early Life: a Celebration of the Work of Martin Brasier*. (Special Publications). Geological Society. DOI: 10.1144/SP448.4

Peer reviewed version

Link to published version (if available):
[10.1144/SP448.4](https://doi.org/10.1144/SP448.4)

[Link to publication record in Explore Bristol Research](#)
PDF-document

This is the accepted author manuscript (AAM). The final published version (version of record) is available online via the Geological Society at <http://doi.org/10.1144/SP448.4>. Please refer to any applicable terms of use of the publisher.

University of Bristol - Explore Bristol Research

General rights

This document is made available in accordance with publisher policies. Please cite only the published version using the reference above. Full terms of use are available:
<http://www.bristol.ac.uk/pure/about/ebr-terms.html>

1 **Advanced analytical techniques for studying the morphology and**
2 **chemistry of Proterozoic microfossils**

3
4 David Wacey^{1,2*}, Leila Battison³, Russell J. Garwood⁴, Keyron Hickman-Lewis⁵, and Martin
5 D. Brasier^{3†}
6

7 1: *Centre for Microscopy Characterisation and Analysis, and Australian Research Council*
8 *Centre of Excellence for Core to Crust Fluid Systems, The University of Western Australia,*
9 *35 Stirling Highway, Perth, WA 6009, Australia.*

10 2: *School of Earth Sciences, University of Bristol, Life Sciences Building, 24 Tyndall Avenue,*
11 *Bristol, BS8 1TQ, U.K.*

12 3: *Department of Earth Sciences, University of Oxford, South Parks Road, Oxford, OX1 3AN,*
13 *U.K.*

14 4: *School of Earth, Atmospheric and Environmental Sciences, University of Manchester,*
15 *Manchester, M13 9PL, U.K.*

16 5: *St Edmund Hall, Queens Lane, Oxford, OX1 4AR, United Kingdom and Department of*
17 *Earth Sciences, Oxford University, South Parks Road, Oxford, OX1 3AN, United Kingdom.*

18 *Present Address: "Homestead", 19 Sunnybank Road, Blackwood, Gwent, NP12 1HT, United*
19 *Kingdom*

20
21 *Correspondence: (David.Wacey@uwa.edu.au)

22 † Deceased
23

24 **Abstract:** This contribution outlines the suite of **advanced** multiscalar techniques in the
25 toolkit of the modern Proterozoic palaeobiologist. These include non-intrusive and non-
26 destructive optical, laser and X-ray based techniques, plus more destructive ion beam and
27 electron beam based methods. Together, these provide morphological, mineralogical and
28 biochemical data at flexible spatial scales from that of an individual atom up to that of the
29 largest of Proterozoic microfossils. Here we provide a description of each technique,
30 followed by a case study from the exceptionally preserved Torridonian biota of Northwest
31 Scotland. This microfossil assemblage was first recognized over a century ago, but its great

32 diversity and evolutionary importance has only recently come to light, due in no small part to
33 the research efforts of Martin Brasier.

34

35 **Running Title:** Proterozoic microfossil techniques

36

37 **Keywords:** MICROFOSSILS–PROTEROZOIC–PRECAMBRIAN EVOLUTION–
38 TORRIDONIAN SUPERGROUP-SCANNING ELECTRON MICROSCOPY–
39 TRANSMISSION ELECTRON MICROSCOPY–X-RAY TOMOGRAPHY–FOCUSSED
40 ION BEAM–LASER RAMAN–CONFOCAL LASER SCANNING MICROSCOPY–
41 SECONDARY ION MASS SPECTROMETRY–3D VISUALISATION

42

43 **INTRODUCTION**

44 Modern palaeobiology primarily exists to discover, describe, and decode the ancient
45 biosphere, and understand the course of global evolutionary change. Stemming from its roots
46 in Victorian natural history, palaeobiology has made good use of technological advances to
47 shed light on new discoveries (see Sutton *et al.* 2014, Wacey, 2014 and references therein),
48 and to reveal previously unimagined details in historical material (Brasier *et al.* 2015). As
49 with any modern field of science, palaeobiological research must continually look forwards
50 to the next potential discovery, utilizing all available tools and techniques.

51

52 Historically, major discoveries have predominantly dated from the Phanerozoic, owing to the
53 relatively well-preserved and easily recovered fossils of the macroscopic organisms alive
54 during this time. In the search for life's origins and early record, attention has inevitably
55 turned to the more poorly understood Proterozoic and Archaean fossil records. The
56 evolutionary history of these expanses of time is much less well established, as a result of the

57 **shortage of exposed rock of appropriate age**, relative paucity of fossil material, and
58 limitations in extracting relevant information. Fossils from these times are typically
59 microscopic, enigmatic, and poorly preserved, although a number of exceptionally preserved
60 deposits have come to characterize the Proterozoic fossil record (e.g. Torridonian biota,
61 **Strother *et al.* 2011**; Doushantuo biota, **Yin & Li 1978**). In both ‘traditional’ and
62 ‘exceptional’ preservation cases, our understanding remains limited by the observational and
63 analytical techniques used to characterize these important specimens.

64

65 The approaches traditionally used to study early fossil material are essentially borrowed and
66 adapted from methods used in the study of Palaeozoic fossils, and are best suited to hard-
67 bodied macroscopic fossils or compressed organic material extracted by acid maceration.
68 However, as our understanding of Precambrian environments is fundamentally improving, it
69 has become clear that entirely different preservational styles are possible, some of which
70 require novel analytical approaches. Although many Proterozoic carbonaceous fossils can
71 still be found compressed within shales (**Javaux *et al.* 2004**; **Agic *et al.* 2015**), and extracted
72 for study by palynological acid maceration techniques, microfossil material can be hosted in
73 a variety of other media, including chert (e.g. Barghoorn & Tyler 1965), pyrite (e.g.
74 Rasmussen 2000), authigenic aluminosilicates (e.g. Wacey *et al.* 2014), and cryptocrystalline
75 phosphate (e.g. Strother *et al.* 2011). These alternative preservational styles originate from
76 the biogeochemical conditions that prevailed in specific environments or across specific
77 periods of time, and are able to exceptionally preserve microfossils of a wide range of
78 affinities in their original spatial context, often in three dimensions, and reflecting a broad
79 spectrum of taphonomic decay. In these cellular lagerstätte, challenges are posed by the small
80 scale, enigmatic nature, and relative scarcity of Proterozoic fossils, as well as by their
81 complex taphonomic and metamorphic histories. Thus, a thorough understanding of

82 Proterozoic and Archaean life necessarily calls for state-of-the-art high-spatial-resolution,
83 and holistic imaging and analysis techniques.

84

85 An increasing number of researchers are now making use of such techniques to study both
86 Proterozoic and Archaean material, revealing unprecedented levels of detail and allowing the
87 reconstruction of the complex Precambrian biosphere. It is still common, however, for these
88 different approaches to be attempted separately, often by different individual research groups,
89 which can partially preclude the synthesis of information and an overall understanding of
90 local, regional, or even global palaeoecologies. Here we present a holistic methodology for
91 studying Proterozoic fossil deposits, with a consideration of their unique preservational styles
92 and histories. A set of complementary microanalysis techniques have already been presented
93 with respect to Archaean material (Wacey 2014). However, with the expansion of the
94 biosphere (Knoll 1994), the evolution of Eukaryotic cells (Knoll *et al.* 2006), and the advent
95 of various metabolic pathways and trophic tiering (Knoll 2015), the Proterozoic fossil record
96 is more complex and - owing to its younger age (approximately 2500–540 Ma) - arguably
97 better preserved. Thus, a greater potential wealth of information might be gleaned from such
98 deposits, necessitating their study on a variety of spatial scales, as well as assessing both
99 morphology and chemistry.

100

101 The following sections detail, in a logical order for practical investigation, multiple
102 approaches for examining a Proterozoic microfossil assemblage, including: ‘traditional’ field
103 study and optical microscopy; X-ray based techniques including X-ray tomography and X-
104 ray spectroscopy; laser-based techniques including Raman spectroscopy and confocal laser
105 scanning microscopy; infrared spectroscopy; electron based techniques including scanning
106 electron microscopy and transmission electron microscopy; and ion based techniques

107 including focused ion beam milling and secondary ion mass spectrometry. The combination
108 of several of these techniques when investigating a single fossil deposit provides the best
109 opportunity to fully reveal the palaeocology of the Proterozoic biosphere. An example of
110 their application to the microfossiliferous rocks of the 1200-1000 Ma Torridonian
111 Supergroup of northwest Scotland is subsequently presented as a demonstrative case study.
112

113 **STANDARD PALAEOBIOLOGICAL TECHNIQUES**

114 **Field Study and Optical Microscopy**

115 A critical starting point for any palaeobiological investigation remains a comprehensive field
116 study and the preparation of candidate material for optical microscopy. As a preliminary
117 investigation, this can provide important palaeoenvironmental context, and enable the
118 quantification of the richness, morphology, and spatial distribution of fossils, plus the
119 depositional setting and taphonomic history of the fossil deposit.

120

121 Initially, a detailed sedimentological and stratigraphic study should be made of the
122 fossiliferous rocks, and those associated with them, to permit accurate palaeoenvironmental,
123 metamorphic, and tectonic interpretation. Such a study will provide regional, local, and fine
124 scale information pertaining to the location, type, and energy of the environment of
125 deposition, as well as any subsequent chemical or structural changes that may have taken
126 place since lithification. Fine scale field observations will also permit the identification of
127 candidate fossiliferous material. This may be related to specific preservational mineralogies,
128 such as cherts (e.g. ~1900 Ma Gunflint Formation; Barghoorn & Tyler 1965) or phosphates
129 (e.g. ~600 Ma Doushantuo Formation; She *et al.* 2013), or be found in association with
130 macroscopic fossil structures including **siliceous and phosphatic** stromatolites (e.g. ~1900 Ma
131 Belcher Supergroup; Hofmann 1976) and microbially induced sedimentary structures (e.g.

132 ~1000 Ma Diabaig Formation; Callow *et al.* 2011). Collection and documentation of
133 candidate material should be methodical, and include GPS localities, orientation data and
134 specific relationships to larger-scale structures.

135

136 From the collected samples, polished, uncovered (which are more useful than covered for
137 subsequent techniques) petrographic thin sections can be prepared for analysis using optical
138 microscopy. Ideally, thin sections should be prepared both perpendicular and parallel to the
139 bedding direction in order to capture the full spatial distribution of microscopic fossils. While
140 sections 30 μm thick are required for mineral identification using cross-polarized light, the
141 detection of fossil material may be facilitated by the use of sections up to $\sim 150 \mu\text{m}$ -thick,
142 provided the encasing medium is sufficiently light-coloured and free of dark impurities. This
143 increases the chances of capturing entire cellular material and in-situ relationships between
144 different fossil taxa.

145

146 The primary purpose of optical microscopy is to locate and identify fossil material, and to
147 document its spatial distribution and relationship with non-biological minerals. For the
148 majority of Proterozoic carbonaceous fossil deposits, examination and imaging at all
149 magnifications up to 1000x is needed to provide a complete context. This can allow the
150 **observation** of fine structural details up to $\sim 0.2 \mu\text{m}$ across, but note at highest resolution oil
151 immersion is required to increase clarity, which may be detrimental to some subsequent
152 techniques. The position of fossil material can be identified and recorded for future reference
153 using standard graticules, When fossil material is preserved with some degree of three-
154 dimensionality, focusing through the thickness of the slide can reveal its shape, organization,
155 and extent. A range of different photomicrography suites are now available for capturing
156 images of such samples (*e.g., Synchrosopy Auto-Montage as demonstrated by Brasier et al.*

157 2005). Many packages contain algorithms for stacking focused images from different depths
158 within a section to produce a single, focused image, or for stitching together images of
159 adjacent fields of view to produce a high-resolution 'map' of a thin section.

160

161 Using a variety of optical micrographic tools, preliminary identification and quantification of
162 fossil material may be carried out, larger-scale spatial relationships determined, and candidate
163 fossils selected for further analysis. This work is vital for the initial study of a fossil deposit
164 but the intrinsic limitations of this approach preclude its use for further, finer-scale analyses.
165 Furthermore, certain media may be unsuitable for investigation by optical microscopy. Dark
166 coloured material, or enclosing media with many impurities, for example, may mask fossil
167 details and reduce their visibility, especially through thick sections. Larger microfossils may
168 be cross cut by the sectioning process, limiting interpretation. Another limitation is that the
169 identification of chemical constituents of samples is limited to that which can be determined
170 by standard petrographic methods, and may not be sufficient for fine-grained or finely-
171 crystalline material. Since carbonaceous fossils are frequently dark-coloured, optical analyses
172 will also only be able to resolve their surface shape and structure, with the fossils themselves
173 masking any underlying ultrastructure or interior features. Thus, for a better understanding of
174 both fossil material and its preservational medium, more versatile high-spatial-resolution
175 techniques are required.

176

177 **Non-destructive moderate to high spatial resolution techniques**

178 Non-destructive techniques are here classified as those which can be applied to a standard
179 geological thin section, rock chip or rock hand sample with minimal further sample
180 preparation and do not consume or alter the specimen of interest during the analysis. Hence,

181 they can be applied to both type specimens (including holotypes on loan from museums) and
182 can be utilized as a precursor to more destructive techniques on newly discovered material.

183

184 *X-ray Computed Tomography (X-ray CT)*

185 X-ray CT maps the X-ray attenuation within a rotating sample. Data is captured as a series of
186 projections that can then be reconstructed as two-dimensional slices and then three-

187 dimensional visualisations (see [Kak & Slaney 2001](#); Cnudde & Boone 2013 for overviews).

188 X-ray attenuation is dictated by factors such as elemental composition and density, hence X-
189 ray CT can often detect variations in the style of fossil preservation and mineralization, as

190 well as building up 3D models of entire specimens ([Conroy & Vannier 1984](#); [Haubitz *et al.*](#)

191 [1988](#); [Sutton *et al.* 2001](#)). The high resolution form of X-ray CT used for fossils is known as

192 X-ray microtomography (μ CT), which has been utilized in palaeobiology for almost two

193 decades ([Rowe *et al.* 2001](#); [Sutton 2008](#)). It is now routinely applied to Phanerozoic

194 vertebrate and invertebrate fossils, ranging for example from echinoderms (Rahman and

195 Zamora, 2009) to dinosaurs ([Brasier *et al.* 2016](#), this volume), and from plants ([Spencer *et al.*](#)

196 2013) to arthropods ([Garwood & Sutton 2010](#)). The study of microfossils using CT has

197 become viable in recent years, with the use of synchrotron-based systems where more

198 intense, monochromatic X-rays, can allow improved contrast and greater spatial resolution

199 ([Donoghue *et al.* 2006](#); [Huldtgren *et al.* 2011](#)). Recent years have also seen improvements in

200 the spatial resolution of lab-based ‘micro-CT’ and ‘nano-CT’ systems where sub- μ m

201 resolutions are now possible ([Hagadorn *et al.* 2006](#); [Schiffbauer *et al.* 2012](#); [Sutton *et al.*](#)

202 2014).

203

204 Despite these technological advances, configuring the correct **instrumental** parameters for

205 μ CT scanning a given microfossil specimen is challenging, and some specimens will not be

206 suited to μ CT due to lack of X-ray attenuation contrast between specimen and matrix **and/or**
207 **presence of X-ray opaque minerals**. In general, μ CT is applied to small rock chips. It is not
208 suited to geological thin sections because of their highly anisotropic nature, although thin
209 sections can be cut down to a more isotropic shape if permitted by the owner, or fossils
210 liberated using a micro-corer. Elsewhere in this volume, Hickman-Lewis *et al.* (2016)
211 provide several case studies of the μ CT scanning of Precambrian microfossil bearing rocks
212 using two lab-based CT scanners with spatial resolutions (minimum voxel sizes) of about
213 $5\mu\text{m}$ and $0.5\mu\text{m}$ respectively. They show that μ CT can be a valuable tool to decode the 3D
214 petrographic context of such biological material, for example, by highlighting potential
215 organic grains and laminations, fractures within the matrix, assemblages of detrital heavy
216 minerals, and replacement of silica by carbonate rhombs (which are known to reduce the
217 quality of microfossil preservation). Detecting individual microfossils using lab-based CT
218 remains challenging unless the preservation window is particularly favourable (e.g. pyritised
219 microfossils in a silica matrix, see Hickman-Lewis *et al.* 2016, this volume). The use of a
220 synchrotron-based CT (or lab-based nano-CT) system can improve matters **by providing**
221 **more intense X-rays and improved spatial resolution**, but this requires more specialist sample
222 preparation (e.g., **micro-coring**) to obtain sub-mm pieces of fossiliferous rock, meaning that it
223 can no longer realistically be classified as a non-destructive technique, and could seldom be
224 applied to holotype material.

225

226 *X-ray Spectroscopy*

227 A logical extension to examining the morphology of microfossils using X-ray
228 microtomography is to investigate their chemistry using X-ray spectroscopy. A range of X-
229 ray techniques are available to characterize fossiliferous rocks, mostly performed on a
230 synchrotron beamline (see Templeton & Knowles 2009; **Fenter *et al.* 2002** for overviews),

231 and utilising both hard X-rays (more penetrating with wavelengths of 1-20 angstroms and
232 photon energies over about 5-10 keV) and soft X-rays (less penetrating with wavelengths of
233 20-200 angstroms and photon energies below about 5 keV). X-ray fluorescence (XRF)
234 mapping provides semi-quantitative element-specific maps over flexible spatial scales (μm to
235 mm; e.g. Edwards *et al.* 2014). Near edge X-ray absorption fine structure (NEXAFS) and X-
236 ray absorption near edge structure (XANES) are spectroscopic techniques, using soft (low
237 energy) and hard (high energy) X-rays respectively, that excite core electrons in an element
238 (Templeton & Knowles 2009). The resulting spectra provide information on both the
239 coordination chemistry and valence of the element of interest. Scanning Transmission X-ray
240 microscopy (STXM) uses soft X-rays to obtain both spectral data and images of this spectral
241 data (e.g., maps of the spatial distribution of specific elements, valence states, or functional
242 groups) at the nm-scale, created by rastering samples through an X-ray beam at stepwise-
243 increasing incident X-ray energies to cover the absorption edges of the elements of interest
244 (e.g., Lawrence *et al.* 2003). Although these types of analyses do not destroy the specimen,
245 specialist sample preparation (e.g., micro-cored rock chips; doubly polished thin sections no
246 more than about 100 μm thick) means that permission for holotype specimens to be analysed
247 in this way is unlikely to be granted. Beam damage can also affect subsequent chemical
248 analyses.

249

250 In terms of Proterozoic microfossils, much of the interest in X-ray spectroscopy surrounds
251 the chemical bonding of carbon. The energy resolution of NEXAFS/XANES is excellent
252 ($\sim 0.1\text{eV}$) so closely spaced peaks can be resolved. Hence, carbon bound, for example, in
253 aromatic groups, aliphatic groups, ketones, peptides, carbonyls, carboxyls and carbonate can
254 all be distinguished from one another (Bernard *et al.* 2007). Such spectra may help
255 characterise cellular versus extracellular organic components, while interfering signals from

256 carbonate minerals can be subtracted. De Gregorio *et al.* (2009) applied this methodology to
257 **powders of** organic material from the 1878 Ma Gunflint Formation, showing that
258 polyaromatic carbon, carboxyl and phenol groups had **all** been preserved in **this ancient**
259 **kerogen**. Similarly, the bonding characteristics of other elements common in organic material
260 (e.g., S, N, P, O) may help to determine whether they are present as organic or inorganic
261 forms in ancient fossiliferous rocks. For example, Lemelle *et al.* (2008) used XRF to quantify
262 the amounts of sulfur within the cell walls of coccooid microfossils from the ~750 Ma Draken
263 Formation, Svalbard, before using XANES to determine sulfur speciation. They showed that
264 the sulfur was a reduced organic form most likely belonging to a thiophene-like compound.

265

266 *Confocal Laser Scanning Microscopy (CLSM)*

267 CLSM provides high-spatial-resolution morphological data (<100 nm is possible) permitting
268 the visualisation of microfossils in three dimensions (see Sutton *et al.* 2014; Halbhuber &
269 **Konig 2003 for overviews**). Under ideal conditions data collection from standard polished or
270 unpolished geological thin sections is rapid and CLSM is able to resolve tiny morphological
271 features that may be unclear or hidden when viewed under light microscopy, as well as
272 giving a true 3D perspective to the distribution of microfossils (Schopf *et al.* 2006; Cavalazzi
273 *et al.* 2011). However, natural samples are rarely ideal for the application of this technique.
274 CLSM relies on the fact that organic material auto-fluoresces when excited by a laser of a
275 specific wavelength. The system can accurately focus and scan at different depths within a
276 microfossil specimen, and exclude the fluorescence from outside the plane of focus; 3D
277 images are then built up combining data acquired from successive planes of focus (see Amos
278 & White 2003). Hence, anything that interferes with the transmission or detection of this
279 signal severely degrades the quality of the final images obtained. For example, specimens
280 situated a long way below the surface of a thin section, or having thick opaque walls will not

281 provide sharp CLSM images. Similarly a specimen surrounded by plentiful fluorescing
282 organic detritus, or embedded in a mineral that internally reflects the fluorescence signal,
283 **may be problematic**. The maturity of the organic material also affects the quality of the data,
284 with the auto-fluorescence signal dissipating as the organic material becomes more
285 geochemically mature and loses more of its heteroatoms (i.e. evolves towards the structure of
286 graphite). Hence, CLSM is of greatest use when applied to thin-walled organic microfossils,
287 preserved in silica (and to a lesser extent phosphate), housed in rocks of low-metamorphic
288 grade. In these cases significant insights into the three-dimensional morphology and
289 taphonomic preservation of Proterozoic microfossils may be obtained. For example in the
290 Neoproterozoic Buxa Formation, CLSM was able to demonstrate the three dimensional
291 organisation of groups of filamentous microfossils (Schopf *et al.* 2008). In the 850 Ma Bitter
292 Springs Formation and the 650 Ma Chichkan Formation notches, tears, grooves and surface
293 ornamentation were all detected in microfossils using CLSM (Schopf *et al.* 2006), while in
294 the ~580 Ma Doushantuo Formation CLSM revealed parts of fibrous tissues and cell walls
295 within fossil alga that were not visible by other means (Chi *et al.* 2006).

296

297 *Laser Raman Microspectroscopy and Imagery*

298 Raman is a versatile, non-intrusive and non-destructive *in situ* technique. It can be used to
299 identify the mineralogy of microfossils and their host rocks, and is particularly sensitive to
300 the molecular structure and geochemical maturity of carbonaceous phases such as kerogen -
301 the prime constituent of organic walled microfossils (see **Beyssac *et al.* 2002** and Fries &
302 Steele 2011 for details). In addition, when utilized in confocal imaging mode, Raman can
303 provide 2D and 3D chemical and structural maps of microfossils at moderate spatial
304 resolution (potentially < 1 μm). Raman can be applied to rock chips and standard uncovered
305 geological thin sections. Data is acquired via laser excitation of the chemical bonds within the

306 sample. This excitation produces characteristic spectra depending on the minerals and
307 compounds present, and maps can be constructed of the spatial distribution of various
308 spectral parameters, including the intensity of a given peak (also sometime referred to as a
309 band), or ratios of two given peaks.

310

311 For the field of Proterozoic palaeobiology, the peaks of interest are often associated with
312 carbon. In perfectly crystalline graphite a single first order peak occurs at 1582 cm^{-1} ,
313 attributed to stretching of the C-C bonds in basal graphite planes (known as the 'G' or
314 'graphite' peak) (Jehlicka *et al.* 2003). Second order peaks occur at $\sim 2695\text{ cm}^{-1}$ and 2735 cm^{-1} .
315 Imperfectly crystallised graphitic carbons including kerogens have additional peaks at
316 $\sim 1355\text{ cm}^{-1}$ (known as the 'D1' or 'disordered' peak) and $\sim 1620\text{ cm}^{-1}$ ('D2'; occurring as a
317 shoulder to the 'G' peak), and a single broad second order peak around 2700 cm^{-1} . The
318 specific position, width and relative intensities of these peaks vary somewhat depending on
319 the degree of ordering of the carbon, and these parameters have been characterised in carbon
320 of varying metamorphic grade in an attempt to use Raman as an indicator of the antiquity of
321 carbon in ancient rocks (Tice *et al.* 2004). This is by no means an exact science, since the
322 starting composition of organic material in different metamorphic terrains, both
323 geographically and temporally, may differ. Putative carbonaceous microfossils should,
324 however, exhibit very similar Raman spectral features as other carbonaceous material in the
325 same rock specimen because both should have undergone the same maturation processes.
326 Raman spectra cannot be used to unequivocally determine the biogenicity of an ancient
327 carbonaceous object because similar spectra to those of biogenic kerogens are seen in
328 laboratory synthesised abiological disordered carbonaceous material (Pasteris & Wopenka
329 2003). However, the co-occurrence of kerogenous composition with features that optically

330 resemble cellular material provides promising preliminary data regarding biogenicity that can
331 be further tested using higher spatial resolution techniques (see below).

332

333 As with CLSM, the highest quality data is obtained from specimens close to the surface of a
334 thin section, and it has been suggested that for viable 3D maps of kerogen to be produced, the
335 entire specimen of interest should be no more than 6-8 μm below the surface (Marshall &
336 Olcott Marshall 2013). The best data will come from specimens lying under translucent
337 minerals such as quartz, $\sim 1\text{-}5\ \mu\text{m}$ below the surface of a thin section; microfossils associated
338 with phases that fluoresce strongly under the laser excitation beam may not provide usable
339 spectra. Care must also be taken not to confuse the carbon signature of interest with that
340 produced by: (i) the polymer used to attach the thin section to the glass slide; (ii) any coating
341 that may have been applied to the section during previous analyses; (iii) overlapping peaks in
342 the vicinity of carbon peaks – of particular note here is the $1320\ \text{cm}^{-1}$ peak of hematite
343 (Marshall *et al.* 2011). The carbon spectrum can also be artificially modified by using too
344 high a laser power, or by analyzing right at the surface of a thin section that has been polished
345 (Fries & Steele 2011). Both of these should always be avoided. Raman can also be used to
346 elucidate some structural information from the minerals that host putative microfossils.
347 Several minerals produce Raman spectral peaks that vary in intensity depending on their
348 crystallographic orientation relative to the incoming laser. This feature can be used, for
349 example, to image the distribution of quartz crystallographic axes to see whether putative
350 microfossil material occurs between grain boundaries, is enclosed by entire grains, or occurs
351 in cracks (Fries & Steele 2011).

352

353 Examples of Raman applied to Proterozoic microfossils include a study by Fries and Steele
354 (2011) who mapped the carbon D/carbon G peak intensity ratio (an indicator of graphite

355 domain size) to show micron-sized variation in the structure of kerogen within and around
356 examples of *Huroniospora* from the 1878 Ma Gunflint Formation. This potentially reflects
357 initial heterogeneities in the biological material. Also within the Gunflint Formation, Wacey
358 *et al.* (2013) used Raman to demonstrate that *Gunflintia* microfossils were dominantly
359 carbonaceous in composition, but were preserved as pyrite in microenvironments where
360 anoxia had permitted pyrite formation via the metabolic activity of sulfate reducing bacteria.
361 Raman has been used extensively by Schopf and colleagues to characterize Proterozoic
362 microfossils (Schopf *et al.* 2005, 2008; Schopf & Kudryavtsev 2005, 2009), culminating in
363 the Raman Index of Preservation (RIP). This correlates the geochemical maturity of the
364 kerogen, the fidelity of microfossil preservation, H/C and N/C ratios of organic material, and
365 the metamorphic grade of the rocks, and includes examples from 22 chert units ranging in
366 age from 400 Ma to 2100 Ma (Schopf *et al.* 2005).

367

368 *Micro-Fourier Transform Infrared Spectroscopy (micro-FTIR)*

369 Micro-FTIR is a vibrational spectroscopy technique that provides complementary
370 information to that obtained from organic material using Raman. In particular, it provides
371 data pertaining to the functional groups attached to carbon chains and their bonding
372 environment within organic material (Mayo *et al.* 2004; Dutta *et al.* 2013; Chen *et al.* 2015).
373 Different peaks in an IR spectrum arise due to different vibrational behaviour in the bonds of
374 groups such as CH₂, CH₃, C-N, C=O and others. FTIR can be applied non-destructively **but**
375 **requires doubly polished thin sections, and the main drawback is currently** the limited spatial
376 resolution obtainable, with recent studies reporting only a ~15 μm² spot size in transmission
377 mode (Qu *et al.* 2015). This is sufficient to characterize larger Proterozoic acritarchs **in**
378 **palynological extracts** (Arouri *et al.* 1999; Marshall *et al.* 2005) and groups of smaller
379 filamentous and coccoid microfossils (Igisu *et al.* 2009), but is insufficient to determine the

380 difference between, for example, wall chemistry and internal chemistry of most Proterozoic
381 organisms. The spatial resolution problem may be circumvented somewhat by using micro-
382 FTIR attached to a synchrotron beamline, where spot sizes of $< 5\mu\text{m}$ have been achieved for
383 some parts of the spectra (Bambery 2016). However, this may require more specialist, **often**
384 **extremely difficult, sample preparation (e.g. $<20\ \mu\text{m}$ thickness, unglued slice).**

385

386 Of particular interest are data from extant microorganisms suggesting that FTIR may provide
387 ‘domain specific’ information, whereby specific components (e.g., lipids) of different
388 domains of life (i.e., prokaryote, eukaryote, and archaea) may possess characteristic ratios of
389 CH_2 and CH_3 groups in their IR spectra (Igisu *et al.* 2009, 2012). This has led to FTIR being
390 used in Proterozoic assemblages in an attempt to decode the phylogenetic affinity of
391 microfossils (Igisu *et al.* 2009, 2014). **The study of Igisu *et al.* (2009) analysed microfossils**
392 **in their mineral matrix and thus concentrated on the CH_x ($2500\text{-}3100\ \text{cm}^{-1}$) region of the**
393 **spectrum.** This type of research is very much in its infancy and a better understanding, both
394 of the changes in CH_2/CH_3 during postmortem alteration processes, and of the spectral
395 parameters of differentiated cells in multicellular organisms, is required in order for these
396 data to become a robust domain level signature. **Insufficient data currently exist for**
397 **comparisons of organic material from different terranes and of different metamorphic grades**
398 **using this technique.** Nevertheless, FTIR analyses from the 850 Ma Bitter Springs Formation,
399 Australia, and 1878 Ma Gunflint Formation, Canada, suggest that organisms in these fossil
400 assemblages belong to Bacteria rather than Archaea or Eukarya (Igisu *et al.* 2009). Likewise,
401 combined FTIR and Raman data from the 1485 Ma Wumishan Formation, China (Qu *et al.*
402 2015), suggests that the organic material here is derived from prokaryote cyanobacteria, and
403 is characterised by a rather homogenous and low CH_3/CH_2 . Finally, FTIR data from
404 acritarchs from the ~ 575 Ma Tanana Formation, Australia, suggest that *Tanarium* are likely

405 eukaryotic micro-algae but *Leiosphaeridia* may be Bacteria (Igisu *et al.* 2009, based on data
406 presented in Marshall *et al.* 2005).

407

408 **Destructive high spatial resolution techniques**

409 *Focused Ion Beam Milling and Scanning Electron Microscopy (FIB-SEM)*

410 SEM has traditionally been of limited use in characterizing Proterozoic microfossils in
411 geological thin sections since the majority of microfossils are embedded within the thin
412 section, and below the reach of this surface-based technique. SEM has, however, provided
413 high spatial resolution morphological data from the surfaces of individual microfossils in acid
414 etched rocks, or those extracted from their host rock using acid maceration. This has
415 revealed, for example, delicate wall ultrastructure that could not be resolved under the light
416 microscope (Javaux *et al.* 2004; Moczydlowska & Willman 2009; Agic *et al.* 2015).

417

418 Recently, the use of SEM in Precambrian palaeobiology has been reinvigorated by a new
419 generation of dual beam instrument, where the user has access to both a focused ion beam
420 (FIB) and an electron beam (see Young & Moore, 2005 for overview). Thus, a highly
421 focused beam of heavy ions (usually Ga⁺) can be used to sputter ions from the sample
422 surface, essentially cutting into the sample with very high (nano-scale) precision (see Wirth
423 2009 for details). The electron beam can be used to image the results. Additional detectors
424 can be inserted to image backscattered electrons (BSE) as well as secondary ones, permit
425 elemental analysis (using an energy dispersive X-ray spectroscopy (EDS) detector), or even
426 phase detection and crystallographic mapping (using an electron backscatter diffraction
427 (EBSD) detector). FIB milling can be used to cut into or through specific features in a thin
428 section or rock chip, allowing the structure perpendicular to the surface to be better visualized
429 (Westall *et al.* 2006). Furthermore, a number of sequential slices can be milled through an

430 object, with images or other data acquired after each slice is milled. The latter is termed FIB-
431 SEM nano-tomography and permits the 3D reconstruction and visualisation of microfossils at
432 very high spatial resolution (see Wacey *et al.* 2012 for details). The resolution attainable is
433 essentially dictated by the size of the object to be analysed in 3D, plus the available time,
434 **although instrumental resolution limits may come into play for very small objects.** Slice
435 thicknesses are set by the user and can be smaller than 50 nm, however, for practical reasons
436 100-200 nm slices have commonly been used. Proterozoic microfossils have been visualized
437 using FIB-SEM nano-tomography from the 1878 Ma Gunflint Formation (Wacey *et al.* 2012,
438 2013), ~1700 Ma Ruyang Group (Schiffbauer & Xiao 2009; **Pang *et al.* 2013**) and ~1000 Ma
439 Torridon Group (see below). In the former, FIB-SEM data were key in revealing
440 heterotrophic bacteria attached to, and **fossilized** in the act of decomposing, larger organisms
441 (Wacey *et al.* 2013). Drawbacks of FIB-SEM nano-tomography include its destructive nature
442 – the analysed specimen is completely consumed and only a digital record of its existence
443 will remain – plus the restrictive timescales involved in both analyzing objects larger than
444 about 30 µm in diameter (**24 hours or more beam-time required**), and in processing and
445 reconstructing the data. A number of options exist for processing and visualizing such data
446 (and data from other 3D techniques such as X-ray CT), ranging from freeware products such
447 as *SPIERS* (serial palaeontological image editing and rendering system; Sutton *et al.* 2012),
448 *Drishti* (Limaye 2012), and *Blender* (Garwood & Dunlop 2014) to more advanced (but
449 expensive) products such as *AVIZO* (www.vsg3d.com). The choice of software will depend
450 on budget, time constraints, quality of the raw data, and whether one is interested in
451 producing just images, or images plus movies (see Sutton *et al.* 2014 for an overview of the
452 options).

453

454 *Transmission Electron Microscopy (TEM)*

455 TEM covers a number of separate sub-techniques that can all be performed in a transmission
456 electron microscope. Most simply, TEM is a very high spatial resolution imaging technique,
457 capable of resolving objects separated by as little as ~ 0.1 nm. A standard TEM image results
458 from variable electron scattering as a beam of electrons is accelerated at high voltage through
459 an ultrathin (ideally ≤ 100 nm) sample; a true high-resolution image (HRTEM) is a phase
460 contrast image with atomic-scale resolution, allowing the visualisation of the arrangement of
461 atoms within a sample (Williams & Carter 2009). This provides information about the
462 crystallinity of a sample, its lattice structure and any defects it may have.

463

464 Sample preparation is key to obtaining high quality data, and in this regard FIB has
465 revolutionized the use of TEM in Precambrian palaeobiology. Before the advent of FIB,
466 sample preparation for TEM involved either grinding up a rock, extracting organic material
467 by acid maceration, or using ion polishing, meaning that the context of the putative
468 microfossils was often lost, it was very difficult to obtain samples of uniform (and ultrathin)
469 thickness, and contamination was widespread. FIB-milling now allows individual
470 microfossils, or even specific parts of individual microfossils to be targeted with great
471 accuracy in their host thin section, then ultrathin wafers (typically about $15 \mu\text{m} \times 10 \mu\text{m} \times$
472 100 nm) can be extracted from below the surface of the thin section (hence eliminating the
473 possibility of contamination) and mounted on a TEM grid (see Wacey *et al.* 2012 for an
474 overview).

475

476 In addition to morphology, a number of other parameters can also be analysed on many
477 TEMs, including elemental composition, bonding and oxidation state, crystal structure
478 (leading to mineral identification), and crystal orientation. The elemental composition of a
479 sample can be determined at the nano-scale using either energy-dispersive X-ray

480 spectroscopy (EDS) or by isolating and mapping specific energy windows from an electron
481 energy loss spectroscopy (EELS) spectrum. The fine structure of peaks within an EELS
482 spectrum can also be used to shed light on the bonding and oxidation state of the element of
483 interest, for example distinguishing disordered carbon from graphite (Buseck *et al.* 1988),
484 and Fe²⁺ from Fe³⁺ (Calvert *et al.* 2005). For advanced crystallography and mineral
485 identification, selected area electron diffraction (SAED) in the TEM provides quantitative
486 information on the distances between atomic planes in crystalline materials, and permits the
487 orientation of several grains of the same mineral to be compared to one another.

488

489 In Proterozoic palaeobiology, TEM has been used for several decades with early images of
490 microfossils extracted from their host rock in the ~850 Ma Bitter Springs Formation,
491 Australia, shown in Oehler (1977). A number of studies have investigated the wall
492 architecture of Proterozoic acritarchs in an attempt to decode their taxonomic affinities,
493 because TEM can detect variations in electron density and texture of different layers within
494 cell walls at nm-scale resolution. These include studies from: the ~575 Ma Tanana
495 Formation, Australia (Aroui *et al.* 1999; Moczydlowska & Willman 2009) where recognition
496 of a trilaminar sheath structure was part of a suite of evidence suggesting the microfossils
497 were chlorophyte algae; the 650 Ma Chichkan Formation, Kazakhstan (Kempe *et al.* 2005)
498 where TEM helped to elucidate the nanostructure of carbon particles making up the cell wall;
499 and the ~1450 Ma Roper and Ruyang Groups of Australia and China respectively (Javaux *et al.*
500 *al.* 2004) where at least four different types of wall ultrastructure suggested a greater
501 diversity of eukaryote clades in these deposits than could have been recognised by standard
502 optical techniques. TEM has also been used to investigate the interplay of microfossil walls
503 with the minerals in which they have been preserved, with studies from the 1878 Ma Gunflint
504 Formation showing how nano-grains of silica disrupt the carbonaceous walls of bacteria as

505 they are fossilized (Moreau & Sharp 2004; Wacey *et al.* 2012), and data from the ~750 Ma
506 Draken Formation, Svalbard, showing both the cell membrane and cytoplasm of the coccoid
507 microfossil *Myxococoides* embedded within nano-grains of silica (Foucher & Westall 2013).
508 Finally, TEM data from the ~580 Ma Doushantuo Formation, China, helped to decode the
509 relationships between preserved microfossils and the phosphate granules in which they are
510 contained and suggested that phosphate precipitation was likely to have been microbially
511 mediated (She *et al.* 2013).

512

513 *Secondary Ion Mass Spectrometry (SIMS)*

514 SIMS as applied to the field of Proterozoic palaeobiology is a surface analysis technique,
515 whereby the elemental or isotopic composition of a sample can be determined at moderate to
516 high spatial resolution and with great sensitivity (i.e. many elements can be detected even
517 when present only at the parts-per-billion level). The surface of a sample is sputtered with an
518 ion beam and the secondary ions ejected from the sample are collected and analysed using a
519 mass spectrometer (see Ireland 1995 for details). Two different types of SIMS instruments
520 are commonly used in in palaeobiological investigations:

521 1) The large radius SIMS, used to accurately determine the stable isotope ratios of key
522 biogenic elements (e.g., carbon, sulfur), plus ratios of radiogenic isotopes in order to date
523 rock formations containing microfossils (see for example Stern *et al.* 2009; Williford *et al.*
524 2013; Farquhar *et al.* 2013). Such instruments can analyse objects as small as ~10-20 μm
525 diameter and the isotopic data can have a precision better than 0.5 parts per thousand (‰).

526 2) The NanoSIMS, which has a different geometry and is thus capable of element (ion)
527 mapping with a lateral resolution down to ~50 nm (see Kilburn & Wacey 2015 for details).
528 The NanoSIMS can also make accurate isotopic measurements from objects smaller than 5
529 μm , albeit with poorer precision (generally >1 ‰) than the large radius SIMS.

530 Both forms of SIMS can be applied to surface features in standard geological thin sections
531 and rock chips, although some specialist sample preparation is needed in order that the
532 sample and appropriate standards can be correctly mounted together within the instrument.
533 This generally involves mounting pieces of thin sections or rock chip alongside analytical
534 standards in resin discs. SIMS is partially destructive in that layers of surface material (as
535 deep as ~200 nm during isotope analysis with large radius SIMS) are consumed during the
536 analysis. Small specimens may be entirely consumed by the analysis, whereas larger
537 specimens can be repolished post analysis to look like new!

538

539 A number of Proterozoic microfossils have been analysed by SIMS in the last 15 years.
540 House *et al.* (2000) were the first to determine the carbon isotope composition of individual
541 microfossils using material from the ~850 Ma Bitter Springs and 1878 Ma Gunflint
542 Formations, finding $\delta^{13}\text{C}$ signatures (-21 to -45 ‰) consistent within specific metabolic
543 pathways (namely the Calvin Cycle and acetyl-CoA). This work was recently refined by
544 Williford *et al.* (2013) who analysed microfossils from four Proterozoic assemblages
545 (Gunflint, Bitter Springs, plus ~650 Ma Chichkan Formation and ~740 Ma Min'yar
546 Formation) with greater precision and reproducibility. They were able to show considerable
547 variability of $\delta^{13}\text{C}$ within individual assemblages that may reflect the preservation of original
548 metabolic differences between different components of each biota, and also potential
549 heterogeneities in molecular preservation in single microfossils. It must be noted at this stage
550 that non-biological reactions are able to produce similar $\delta^{13}\text{C}$ fractionations (McCollom &
551 Seewald 2006), so a $\delta^{13}\text{C}$ value must be supported by a definitive biological morphology in
552 order to prove the biogenicity of ancient carbonaceous objects.

553

554 SIMS has also been used to investigate metabolic pathways involving sulfur in Proterozoic
555 organisms. Wacey *et al.* (2013) determined the $\delta^{34}\text{S}$ composition of pyritised microfossils
556 from the 1878 Ma Gunflint Formation, finding sulfur fractionations ($\delta^{34}\text{S} = +7$ to $+22$ ‰)
557 consistent with pyrite formation via the activity of sulfate reducing bacteria in sulfate starved
558 sediment porewaters. In the same study, Wacey *et al.* (2013) used NanoSIMS to map the
559 residual carbon and nitrogen associated with the pyritised microfossils and found
560 reproducible differences in the preservation of organic material between two different types
561 of organism (*Huroniospora* versus *Gunflintia*). *Gunflintia* was poorly preserved which
562 suggests that it was more prone to decay by heterotrophic bacteria (that also mediated pyrite
563 formation) than *Huroniospora*. NanoSIMS mapping of organic microfossils in the ~850 Ma
564 Bitter Springs Formation has shown the co-occurrence of carbon, nitrogen and sulfur in such
565 microstructures (Oehler *et al.* 2006) and attempts have been made to quantify the ratios of
566 nitrogen and carbon (N/C) to distinguish different components of microbial communities, or
567 to distinguish biology from co-occurring abiotic organic material (Oehler *et al.* 2009;
568 Thomen *et al.* 2014) although the SIMS community has yet to agree upon the robustness of
569 these methods.

570

571 **A PROTEROZOIC CASE STUDY: THE 1200-1000 MA TORRIDONIAN LAKES**

572 The effectiveness of combining multiple high-spatial-resolution, *in-situ* techniques is
573 demonstrated here using a case study of microfossils from the 1200-1000 Ma Torridonian
574 Supergroup of Northwest Scotland. Not all techniques described above were applied to the
575 Torridonian material in order to avoid duplication of data and in order to keep costs and
576 processing time to reasonable levels. For example, we felt in this case that higher quality 3D
577 morphological data could be acquired using FIB-SEM rather than CLSM, and that detailed
578 chemistry could be better (and more cheaply) determined using TEM rather than X-ray

579 spectroscopy. Below we present data obtained from light microscopy, SEM, μ CT, laser
580 Raman, NanoSIMS, TEM and FIB-SEM nano-tomography which together provide a detailed
581 characterisation of a number of components of the Torridonian biota.

582

583 **Methods**

584 *Optical microscopy*

585 Polished and uncovered petrographic thin sections of 30 μ m and 100 μ m thickness were
586 examined under *Nikon Optiphot-Pol* and *Nikon Optiphot-2* microscopes with 4x, 10x, 20x,
587 40x and 100x (oil immersion) lenses at the Department of Earth Sciences, University of
588 Oxford, and with a *Leica DM2500M* microscope with 4x, 10x, 20x and 50x lenses at the
589 Centre for Microscopy Characterisation and Analysis (CMCA), The University of Western
590 Australia. Images were captured using *Synchroscope* imaging software (*Acquis* and *Auto-*
591 *montage*) at Oxford, and using *Toupview* imaging software at CMCA. Post processing, for
592 example colouring of cells in Figures 2 and 3, was carried out in *Adobe Photoshop* (*GIMP* is
593 an open source alternative).

594

595 *SEM analysis of palynological specimens*

596 Palynological samples were prepared at the Department of Animal and Plant Sciences,
597 University of Sheffield, using conventional acid maceration techniques (Grey 1999).
598 Following HCl-HF-HCl acid maceration, the residues were sieved using a 10 μ m mesh. They
599 were then treated to a heavy liquid separation using zinc chloride, followed by further sieving
600 at 10 μ m. The organic residues were mounted directly onto glass slides using epoxy resin.
601 SEM imaging was carried out using a *JEOL JSM-840A* SEM located at the Department of
602 Earth Sciences, University of Oxford.

603

604 *X-ray μ CT*

605 CT scans were performed at the Manchester X-ray Imaging Facility using: a *Nikon Metris*
606 225/320 kV X-ray CT system in a customized bay (tungsten reflection target; current/voltage
607 of 130 μ A/80kV; no filtration; 3142 projections of 708 ms exposure collected with a 2000 \times
608 2000 detector; reconstructed dataset 5.1 μ m voxels); and a *Zeiss Xradia Versa 520* (standard
609 transmission target; current/voltage of 62 μ A/160kV; standard in-built, high energy 2 Zeiss
610 filter; 4x optical magnification, 501–1001 projections of exposures between 0.5 and 2
611 seconds, collected with 4x binning using a 2000 x 2000 detector; reconstructed datasets with
612 1–2 μ m voxel size). Additional propagation-based phase-contrast scans were performed at the
613 TOMCAT beamline of the Swiss Light Source (Paul Scherrer Institut, Villigen, Switzerland;
614 1001 projections of 700ms exposure; 37 KeV monochromatic beam; 4x objective; a LAG:Ce
615 100 μ m scintillator; reconstructions based on both attenuation and phase used to create
616 datasets with 1.625 μ m voxels). Datasets were reconstructed using the *SPIERS* software suite
617 (Sutton *et al.* 2012) following the methods of Garwood *et al.* (2012), and *Drishti* (Limaye
618 2012) following the methods of Streng *et al.* (in press).

619

620 *Laser Raman*

621 Laser Raman analyses were carried out at the University of Bergen using a *Horiba LabRAM*
622 *HR800* integrated confocal Raman system and *LabSpec5* acquisition and analysis software.
623 Samples were standard uncovered geological thin sections allowing optical and chemical
624 maps to be superimposed. All analyses were carried out using a 514.5 nm laser, 100 μ m
625 confocal hole, 1800 grating and 50x objective lens. The laser was focused at least 1 μ m
626 below the surface of the thin sections to avoid surface polishing effects. For mineral
627 identification from Raman spectra, dual acquisitions were taken from each analysis point,

628 each with an acquisition time of 4 s. Raman maps were acquired with a 1.5 μm spatial
629 resolution.

630

631 *TEM of FIB-milled wafers*

632 TEM wafers were prepared using two dual-beam FIB system (*FEI Nova NanoLab*) at the
633 Electron Microscopy Unit (EMU) of the University of New South Wales (UNSW), and
634 Adelaide Microscopy at the University of Adelaide. Electron beam imaging was used to
635 identify microfossils of interest in standard polished thin sections coated with c. 30 nm of
636 gold, allowing site-specific TEM samples to be prepared. The TEM sections were prepared
637 by a series of steps involving different Ga^+ ion beam energies and currents (see Wacey *et al.*
638 2012), resulting in ultrathin wafers of c. 100 nm thickness. These TEM wafers were either
639 attached to *Omniprobe* copper TEM holders or deposited on continuous-carbon copper TEM
640 grids. TEM data were obtained using a *FEI Titan G2 80-200* TEM/STEM with *ChemiSTEM*
641 *Technology* operating at 200 kV, plus a *JEOL 2100* LaB_6 TEM operating at 200 kV equipped
642 with a *Gatan Orius* CCD camera and *Tridiem* energy filter. Both instruments are located in
643 CMCA.

644

645 *NanoSIMS*

646 Ion mapping was performed using a CAMECA NanoSIMS 50 at CMCA, with instrument
647 parameters optimized as described in Wacey *et al.* (2011). Analysis areas were between 12 x
648 12 μm and 25 x 25 μm with a resolution of 256 x 256 pixels (so each pixel measures between
649 47 nm and 98 nm), with a dwell time of 5-15 ms per pixel, and a primary beam current of
650 ~ 2.5 pA. Secondary ions mapped were $^{24}\text{C}_2^-$, $^{12}\text{C}^{14}\text{N}^-$, $^{28}\text{Si}^-$, $^{32}\text{S}^-$, and $^{56}\text{Fe}^{16}\text{O}^-$, and charge
651 compensation was achieved by using the electron flood gun.

652

653 *FIB-SEM nano-tomography*

654 Sequential FIB milling and SEM imaging was carried out on a *Zeiss Auriga Crossbeam*
655 instrument at the Electron Microscopy Unit of UNSW, using the method of Wacey *et al.*
656 (2012, 2014). Key parameters were adjusted to suit the specific size and nature of each
657 sample of interest. In summary: initial trenches were milled using a 9 nA beam current; the
658 imaged face was cleaned using a 2 nA beam current; ion beam current for slice milling was 2
659 nA; electron beam voltage for imaging varied between about 800 V and 5 kV; step sizes
660 between slices were between 75 nm and 200 nm; and image capture times were around 30
661 seconds per frame. In some cases, dedicated trenches were milled in order to obtain elemental
662 (EDS) maps of microfossils that were not subsequently milled for 3D analysis.

663

664 In order to visualize the data, FIB-SEM images were stacked, aligned and cropped using
665 *SPIERSalign* (Sutton *et al.* 2012). The resultant stacks were imported into *SPIERSedit*
666 (Sutton *et al.* 2012) where a number of masks were added to segment individual components
667 (e.g., cell walls, cell contents) of the microfossil assemblage. The resulting files were
668 exported and loaded into *SPIERSview* (Sutton *et al.* 2012) to generate the 3D surface
669 renderings.

670

671 **Results**

672 Critically, before the Torridonian microfossils were subjected to the high-spatial-resolution,
673 *in situ* microanalysis described here, multiple seasons of fieldwork had been completed in
674 order to gain a firm understanding of the geological context of the host rocks. In addition,
675 over 100 thin sections and hand samples had been studied in order to understand the
676 depositional context and post-depositional history of the rocks, and to isolate only the very
677 best and most promising samples for further study. A large amount of optical microscopy

678 work had also been completed in order to form an estimate of the morphological diversity of
679 the biota. This work has all been peer reviewed and published (Strother *et al.* 2011; Callow *et*
680 *al.* 2011; Battison & Brasier 2012; Strother & Wellman, 2015) thus giving a firm platform on
681 which to build with this high-resolution work. A summary of some of the most common
682 components of the Torridonian biota as observed by optical microscopy is given in Figure 1
683 for reference.

684

685 *SEM data*

686 As may be expected, the range of morphologies visible in SEM analysis (Fig. 2) is broadly
687 comparable to those observed within thin sections of the phosphate (Fig. 1, plus Battison &
688 Brasier 2012). Many simple vesicles and tubular morphotypes are observed, with SEM
689 imaging affording enhanced resolution of their shape and wall structure. In particular,
690 differences in the physical responses of structures to compression hint at differences in cell
691 wall architecture. Two principal wall responses are observed. Thicker walled (wall at least 1
692 μm thick) specimens accommodate flattening with broad rounded velvet-like folds, or large
693 creases (Fig. 2a). In contrast, thin-walled vesicles ($<0.5 \mu\text{m}$) accommodate compression with
694 fine wrinkles irregularly distributed across the surface, and are apparently more prone to
695 small tears (Fig. 2b). The flattening of these walls during preparation does not permit
696 resolution of any ultrastructural lamination, but synthesis of taphonomic response and wall
697 thickness may be used to enhance interpretation of microfossils studied by optical
698 microscopy.

699

700 A number of unique forms of microfossils are also observed in SEM. This is likely due to the
701 processing of larger quantities of material during preparation by acid maceration, as well as
702 the enhanced resolution afforded by SEM imaging. Of note are two morphotypes, the first

703 (Fig. 2c) comprising a vesicle around 50 μm in diameter, ornamented with regular pits
704 around 10 μm across, with each pit possessing a raised 'collar' approximately 2 μm wide and
705 2 μm high. This form bears some resemblance to the basal vesicle of *Cheilofilum*
706 *hysteriopsis* Butterfield (see Butterfield, 2005 fig. 8 and fig. 10) or the freshwater green
707 microalga *Botryococcus braunii* (see Vandenbroucke & Largeau 2007 plate e) in its
708 possession of flanged openings. The second form (Fig. 2d) is a spherical hollow vesicle
709 around 20 μm in diameter, with a spongy textured wall, and irregularly distributed, rounded
710 or sub circular holes \sim 1-3 μm across. This morphotype is particularly notable for its retention
711 of three-dimensional structure following maceration, indicating significant rigidity of the
712 wall. In addition, distributed abundantly amongst the structurally distinguishable vesicles and
713 sheaths, is non-vesicular membranous organic matter, with an irregularly pustulate and pitted
714 texture, and an amorphous architecture. The size and nature of this material is likened to the
715 amorphous extra-polymeric substances (EPS) secreted by mat-forming organisms in modern
716 microbial ecosystems (cf. Paction *et al.* 2007), but could also be amorphous kerogen. This
717 material is occasionally seen contained within thin sections as a light-walled membrane, but
718 its texture and extent is clearer under SEM analysis.

719

720 Of particular note, amongst the vesicles, sheaths and putative EPS are small coccoid or
721 bacillate forms seen to be colonizing, to varying degrees, some of the larger fossil structures.
722 These are associated with pits within those larger structures, and are apparently embedded
723 within a membrane that links them to the host fossil (Fig. 3). We interpret these forms as
724 fossils of heterotrophic bacteria preserved feeding on the larger Torridonian microbial flora,
725 and this interpretation reinforces observations made previously using light microscopy (see
726 Battison and Brasier, 2012, fig.9, where evidence for heterotrophy includes roughly circular

727 holes in large microfossil vesicles and inferred clumps of heterotrophic bacteria
728 pseudomorphing decayed vesicles).

729

730 *X-ray μ CT data*

731 Microtomography was explored as a method to investigate the petrographic context of
732 cellular material and was also tested in order to determine whether individual microfossils
733 could be detected and their 3D morphology characterized. Scans of rock chips from the
734 Cailleach Head Formation using a *Nikon Metris 225/320* kV X-ray CT system with 5.1 μ m
735 voxels revealed phosphate nodules as a slightly denser phase that could be distinguished from
736 the surrounding matrix sediment (Fig 4a, purple). It also suggested that phosphate was
737 present in small quantities close to, but exterior to the main nodule. Rounded concentrations
738 of a very dense phase, most likely to be an iron rich mineral such as pyrite or iron oxide, were
739 shown to be present both within and outside the nodule (Fig. 4a, gold). Hence, CT could be
740 employed in future investigations as a pre-screen of rock fragments in order to determine the
741 best position within the rock to cut thin sections. Within the phosphate nodules, the *Nikon* CT
742 scans detected phases of lower density that may be organic microfossils. However, the spatial
743 resolution of this instrument was insufficient to determine if these lower density objects were
744 indeed microfossils or simply lower density sediment grains (e.g. quartz) scattered through
745 the phosphate nodules. Higher resolution scans of a different rock chip (with 1.625 μ m
746 voxels) conducted at the Swiss Light Source demonstrate a complex sedimentary texture -
747 here both phosphate and other dense phases are present in the form of evenly spaced
748 rounded- to angular- fragments within the scanned rock chips (Fig. 4b), with no evidence of
749 well-formed nodules of phosphate. The lack of evidence for nodules suggest that this rock
750 chip would not be a promising target for further investigation of microfossils.

751

752 CT scans of a sub-portion of the sample examined in the *Nikon* instrument, performed using a
753 *Zeiss Xradia Versa 520* with voxels of c. 1.5 μm detected a small number of low density
754 objects that strongly resemble microfossils observed in thin sections (Fig. 4c-d, f-g). These
755 objects are analogous to some of the largest and darkest-walled vesicles seen in thin sections
756 (Fig. 4e, h) and CT permits their viewing from multiple orientations in 3D space. These
757 putative fossils are also frequently found close to the very high density phases (presumably
758 iron oxide or pyrite). The combined evidence suggests that μCT at this resolution is only
759 capable of detecting the largest and thickest-walled components of the Torridonian biota. We
760 also suggest that the increased density contrast when such fossils occur in close proximity to
761 iron oxide or pyrite aids detection by CT. The remaining components of the biota (e.g.
762 examples shown in Fig. 1) are essentially invisible on X-ray CT scans conducted at these
763 resolutions. The biggest challenge for future work will be identifying workflows to isolate
764 known microfossils for future scanning.

765

766 *Raman data*

767 Raman data inform upon the dominant mineralogy of the Torridonian microfossils and their
768 surrounding matrix, plus the structure and thermal history of any organic carbon present.
769 Raman maps from the Cailleach Head Formation (Fig. 5a-c) demonstrate that the
770 microfossils are indeed carbonaceous (Fig. 5b) and that the dominant fossilizing phase is
771 apatite (Fig. 5c). Raman also shows that intracellular inclusions (Fig. 5a arrows), common in
772 many of the spheroidal fossils from this formation, are also carbonaceous in composition.
773 Hence, these inclusions likely represent plasmolysed (shrunken) cell contents or, in some
774 cases, could represent a fossilised cell nucleus. Raman spectrum in the first order region of
775 carbon, show the two main bands (D1 at about 1350 cm^{-1} and G at about 1600 cm^{-1})
776 characteristic of disordered carbonaceous material. The D1 band is very broad (full width at

777 half peak maximum (FWHM) of $\sim 120 \text{ cm}^{-1}$) with a shoulder at its low wavenumber side.
778 This shoulder is caused by a small band at $\sim 1150 \text{ cm}^{-1}$ which is only observed in very
779 disordered carbonaceous material (Marshall *et al.* 2005). The G band appears to have been
780 shifted considerably from its value in crystalline graphite (1582 cm^{-1}) to a value of $\sim 1610 \text{ cm}^{-1}$.
781 This reflects an overlap of the G band with a well-developed disorder band (D2) at ~ 1620
782 cm^{-1} . The spectrum indicates that the carbonaceous material has very weak structural
783 organization, has experienced little or no metamorphism (cf. Wopenka & Pasteris 1993), and
784 is consistent with previously suggested maximum heating of only $\sim 100 \text{ }^\circ\text{C}$ (Stewart & Parker
785 1979).

786

787 Not all microfossils are preserved purely as carbon. In the Stoer Group, Raman reveals that
788 significant portions of microfossil walls have been pyritised, although some carbonaceous
789 signal remains (Fig. 5d-f). The matrix mineralogy is also different here, with typical phases
790 including calcite and albitic feldspar (Fig. 5g-h). These data indicate that different suites of
791 lakes within the Torridonian had different chemistries, with those of the Stoer Group being
792 sulphate-rich and phosphate-poor compared to those of the Cailleach Head and Diabaig
793 Formations (see Parnell *et al.* 2016, this volume, for further details on contrasting fossil
794 preservation in these lakes).

795

796 *NanoSIMS data*

797 NanoSIMS was used as an additional tool to determine whether the microfossils were
798 composed of carbonaceous material and then to determine if any additional elements of
799 biological interest were preserved within their cell walls or intracellular space. NanoSIMS
800 uniquely revealed significant (but not quantifiable) amounts of nitrogen and sulfur within
801 cellular material from the Diabaig Formation (Fig. 6). These data were collected from FIB-

802 milled wafers and so the nitrogen and sulfur come from cell walls located below the surface
803 of a thin section; this negates the possibility that these biological signals come from surface
804 contamination and provides an improvement on previous NanoSIMS methodology where
805 such ion mapping was performed on surface features (e.g. Oehler *et al.* 2006, 2009). The co-
806 occurrence of C, N and S in microstructures that have cellular morphology is strong evidence
807 of the biogenicity of such structures; while this is less relevant to the Torridonian material
808 whose biogenicity is well accepted, it is a very useful tool for the investigation of older
809 and/or more controversial fossil material. Building up a database of the C, N and S
810 concentrations of different types of organic material may also be useful in the future to help
811 determine if different components of cells (i.e. wall, membrane, nucleus, cytoplasm) can be
812 preserved in exceptional circumstances. NanoSIMS also revealed the nature of some non-
813 carbonaceous intracellular inclusions within the Diabaig Formation; in optical microscopy
814 these inclusions are ruby red in colour (Fig. 6a), and NanoSIMS shows that they are iron
815 oxides (Fig. 6e-f) and at least some occur in direct contact with the inner cell wall. These
816 inclusions are rare, found in <1% of Torridonian microfossils, but may indicate a unique
817 intracellular chemistry in this small proportion of specimens.

818

819 *TEM data*

820 TEM data reveal the chemistry of the fossilizing mineral phases and the ultrastructure of the
821 microfossils at a spatial scale (nm) unattainable by any other technique. For example,
822 ChemiSTEM (**STEM-EDS**) elemental mapping combined with selected area electron
823 diffraction has shown that phosphate is not necessarily the dominant mineral responsible for
824 exceptional microfossil preservation in the Cailleach Head and Diabaig Formations (cf.
825 Raman and optical data). In fact, the minerals immediately adjacent to most vesicle walls are
826 Fe-rich clay minerals of the chlorite group or K-rich clay minerals approximating illite (Fig.

827 7; see Wacey *et al.* 2014 for details on clay mineral identification); phosphate only dominates
828 at some distance (tens to hundreds of nm) away from the cellular material. The interior of
829 many microfossils are also filled with K-rich clay minerals (Fig. 7), although phosphate
830 grains are also common in many cell interiors (e.g., Wacey *et al.* 2014, fig. 8). STEM-EDS in
831 the TEM detects small C and F peaks in the phosphate spectra confirming that the phosphate
832 is the common low temperature form often associated with fossils, francolite (carbonate
833 fluorapatite).

834

835 TEM imaging reveals sub-components of microfossil walls that were not previously
836 recognized. In many cases a presumed single, thick vesicle wall is shown to comprise
837 multiple components. These can include a thicker inner wall sitting within a thinner outer
838 wall, perhaps suggesting a cyst housed within a vegetative cell, or even more complex
839 arrangements of up to four distinct layers within a 'wall zone' (Fig. 7). Such arrangements
840 are too complex for simple prokaryote cells. Hence, this strongly suggests a eukaryotic
841 component to the biota. These complex layered walls are also preserved in clay minerals.
842 Hence, the combined data suggest that the fidelity of microfossil preservation may be
843 enhanced by early precipitation of clay minerals, and that microfossil preservation in clay
844 minerals may be of even higher quality than in phosphate.

845

846 *FIB-SEM data*

847 Two types of data were acquired using FIB-SEM, chemical and 3D morphological. Chemical
848 data were acquired by simply slicing into a microfossil using a FIB and then analyzing the
849 chemistry of a cross section through the microfossil using SEM-EDS. This provided similar
850 data to STEM-EDS in the TEM but at a more flexible spatial scale (i.e. could be applied to
851 larger fossils, albeit at lower spatial resolution). These data reinforced those acquired using

852 TEM, showing that in fossils with complex walls (interpreted as eukaryotes) clay minerals
853 occurred in direct contact with microfossil walls, in between multiple walls, and in
854 microfossil interiors, while calcium phosphate tended to occur exterior to the fossil (Fig. 8).
855 In simpler prokaryote fossils, the pattern was less defined, with phosphate mixed with clay
856 minerals typically occurring both exterior and interior to the cell (Fig. 9a-b).

857

858 Morphological data in three dimensions were acquired using FIB-SEM nano-tomography
859 whereby sequential FIB slicing was followed by imaging using the SEM (see methods
860 above). This provided an excellent visualization of cellular material located below the surface
861 of the thin section (Fig. 9b) that would otherwise have been hidden by overlying fossil
862 material (Fig. 9a). In addition, individual cells and cell contents could be visualized from
863 multiple orientations in 3D space (Fig. 9c-f). This is particularly useful for accurately
864 locating the position of organic intracellular inclusions (Fig. 9c-f). In the example presented
865 here these inclusions are most likely shrunken remnants of the cytoplasm of simple
866 prokaryote cells, but in future it may be possible to detect the remnants of eukaryotic nuclei
867 or organelles, if preserved using such methods.

868

869 **CONCLUSIONS**

870 Here we have provided an overview of the types of high-resolution techniques currently
871 available to those interested in characterizing Proterozoic microfossils and their associated
872 minerals and fabrics. Techniques have been classified either as non-destructive, hence
873 applicable to all material including holotypes, or destructive, hence applicable in cases where
874 conservation of the specimen is not a requirement. Non-destructive techniques include laser
875 Raman, CLSM, SEM, infrared spectroscopy, X-ray CT and X-ray spectroscopy, although to
876 obtain the highest spatial resolution data using the latter two methods, specialized (and partly

877 destructive) sample preparation is required. Destructive techniques include SIMS where the
878 surface layers of a microfossil are sputtered away during analysis, TEM where an ultrathin
879 slice must be extracted from the microfossil, and FIB-SEM nano-tomography which
880 consumes the entire specimen during analysis.

881

882 Maximum information is gained by the consilience of multiple approaches to a microfossil
883 assemblage, but in reality there will be some tradeoff between time and budget constraints,
884 efforts to conserve the best specimens, and the spatial resolution required. The destructive
885 techniques of TEM and FIB-SEM provide the greatest spatial resolution while SIMS
886 uniquely provides isotopic data. A sensible workflow would involve analysis of petrographic
887 context and a significant number of representative specimens using non-destructive avenues,
888 followed by focused analysis of fewer specimens by destructive means.

889

890 A case study from the Torridonian of northwest Scotland, a microfossil assemblage whose
891 importance has recently been highlighted by work led by Martin Brasier, demonstrated the
892 additional insights that these high resolution techniques can offer. Microtomography
893 provided a rapid way to determine the locality of phosphate nodules that house microfossils,
894 and other petrological details. SEM revealed a number of new morphotypes not previously
895 recognized in optical work and hinted at different taphonomic responses by different types of
896 cell and vesicle walls. TEM revealed the fine scale distribution of mineral phases in and
897 around cellular material, and showed that clay minerals played an important part in the
898 exceptional preservation of this biota. Raman together with NanoSIMS revealed details of the
899 organic material making up the cells, including its thermal maturity and biochemistry in
900 terms of C, N and S content. Finally, FIB-SEM nano-tomography provided a detailed 3D

901 view of a number of fossilized cells, including the location of the remains of organic cell
902 contents.

903

904 **ACKNOWLEDGMENTS**

905 We acknowledge the facilities, scientific and technical assistance of the Australian
906 Microscopy & Microanalysis Research Facility at: Centre for Microscopy Characterisation
907 and Analysis, The University of Western Australia; Electron Microscopy Unit, The
908 University of New South Wales. These facilities are funded by the Universities, State and
909 Commonwealth Governments. We acknowledge the following for technical assistance: Matt
910 Kilburn and Paul Guagliardo for assistance with NanoSIMS; Martin Saunders for assistance
911 with TEM; Charlie Kong for assistance with FIB; Phil Withers, and the Manchester X-ray
912 Imaging Facility, which was funded in part by the EPSRC (grants EP/F007906/1,
913 EP/F001452/1 and EP/I02249X/1); Nicola McLoughlin for access to the University of
914 Bergen laser Raman facility; Owen Green for thin section preparation and access to the
915 Oxford University SEM; Imran Rahman, Alan Spencer, Jonny Waters, and Nidia Alvarez for
916 assistance on beamtime, and the Paul Scherrer Institut, Villigen, Switzerland for the provision
917 of synchrotron radiation beamtime on the TOMCAT beamline at the Swiss Light Source; and
918 Charles Wellman for acid maceration of microfossils. DW was funded by the European
919 Commission and the Australian Research Council (FT140100321). RG is a Scientific
920 Associate at the Natural History Museum, London, and a member of the Interdisciplinary
921 Centre for Ancient Life (UMRI). This is CCFS paper XXX (to be inserted after acceptance).
922 We thank Kevin Lepot and James D. Schiffbauer for their review comments that improved
923 the quality of this manuscript.

924

925 **REFERENCES**

- 926 Agic, H., Mocztdlowska, M. & Yin, L.-M. 2015. Affinity, life cycle, and intracellular
927 complexity of organic-walled microfossils from the Mesoproterozoic of Shanxi, China.
928 *Journal of Paleontology*, **89**, 28-50.
929
- 930 Amos, W.B. & White, J.G. 2003. How the confocal laser scanning microscope
931 entered biological research. *Biology of the Cell*, **95**, 335-342 .
932
- 933 Arouri, K., Greenwood, P.F. & Walter, M.R. 1999. A possible chlorophycean affinity of
934 some Neoproterozoic acritarchs. *Organic Geochemistry*, **30**, 1323-1337.
935
- 936 Bambery, K.R. 2016. Synchrotron infrared micro-spectroscopy of single cells at the
937 Australian Synchrotron. Abstracts of the 24th Australian Conference on Microscopy and
938 Microanalysis, Melbourne, Australia, 31st Jan – 4th Feb 2016.
939
- 940 Barghoorn, E.S. & Tyler, S.A. 1965. Microorganisms from the Gunflint Chert.
941 *Science*, **147**, 563-577.
942
- 943 Battison, L. & Brasier, M.D. 2012. Remarkably preserved prokaryote and eukaryote
944 microfossils within 1 Ga-old lake phosphates of the Torridon Group, NW Scotland.
945 *Precambrian Research*, **196-197**, 204-217.
946
- 947 Bernard, S, Benzerara, K. & Beyssac, O. 2007. Exceptional preservation of fossil plant
948 spores in high-pressure metamorphic rocks. *Earth and Planetary Science Letters*, **262**, 257-
949 272.
- 950
- 951 Beyssac, O., Goffe, B., Chopin, C. & Rouzard, J.N. 2002. Raman spectra of carbonaceous
952 material in metasediments: a new geothermometer. *Journal of Metamorphic Geology*, **20**,
953 859-871.
954
- 955 Brasier, M.D., Green, O.R., Lindsay, J.F., McLoughlin, N., Steele, A. & Stoakes, C. 2005.
956 Critical testing of Earth's oldest putative fossil assemblage from the ~3.5 Ga Apex chert,
957 Chinaman Creek, Western Australia. *Precambrian Research*, **140**, 55-102.
958
- 959 Brasier, M., Antcliffe, J., Saunders, M., & Wacey, D. 2015. Changing the picture of Earth's
960 earliest fossils (3.5-1.9 Ga) with new approaches and new discoveries. *Proceedings of the*
961 *National Academy of Sciences USA*, **112**, 4859-4864.
962
- 963 Brasier, M.D., Norman, D.B., Liu, A.G., Cotton, L.J., Hiscocks, J., Garwood, R.J., Antcliffe,
964 J.B. & Wacey, D. 2016. Remarkable preservation of brain tissues in an Early Cretaceous
965 iguanodontian dinosaur. *Journal of the Geological Society London* (this volume).
966
- 967 Buseck, P.R., Bo-Jun, H. & Miner, B. 1988. Structural order and disorder in Precambrian
968 kerogens. *Organic Geochemistry*, **12**, 221-234.
969
- 970 Butterfield, N.J. 2005. Reconstructing a complex early Neoproterozoic eukaryote, Wynnatt
971 Formation, Arctic Canada. *Lethaia*, **38**, 155-159.
972
- 973 Callow, R., Battison, L. & Brasier, M.D. 2011. Diverse microbially induced sedimentary
974 structures from 1 Ga lakes of the Diabaig Formation, Torridon Group, northwest Scotland.
975 *Sedimentary Geology*, **239**, 117-128.

976
977 Calvert, C.C., Brown, A. & Brydson, R. 2005. Determination of the local chemistry of iron in
978 inorganic and organic materials. *J. Elec. Spect. Rel. Phenom.*, **143**, 173-187.
979
980 Cavalazzi, B., Westall, F., Cady, S.L., Barbieri, R. & Foucher, F. 2011. Potential fossil
981 endoliths in vesicular pillow basalt, Coral Patch Seamount, eastern North Atlantic Ocean.
982 *Astrobiology*, **11**, 619-632.
983
984 Chen, Y., Zou, C., Mastalerz, M., Hu, S., Gasaway, C. & Tao, X. 2015. Applications of
985 micro-fourier transform infrared spectroscopy (FTIR) in the geological sciences – a review.
986 *International Journal of Molecular Sciences*, **16**, 30223-30250.
987
988 Chi., H., Xiao, Z., Fu, D. & Lu, Z. 2006. Analysis of fluorescence from algae fossils of the
989 Neoproterozoic Doushantuo Formation of Chian by confocal laser scanning microscope.
990 *Microscopy Research and Technique*, **69**, 253-259.
991
992 Cnudde, V. & Boone, M.N. 2013. High-resolution X-ray computed tomography in
993 geosciences: A review of the current technology and applications. *Earth-Science Reviews*,
994 **123**, 1-17.
995
996 Conroy, G.C. & Vannier, M.W. 1984. Noninvasive three-dimensional computer imaging of
997 matrix-filled fossil skulls by high-resolution computed tomography. *Science*, **226**, 456-458.
998
999 De Gregorio, B.T., Sharp, T.G., Flynn, G.J., Wirrick, S. & Hervig, R.L. 2009. Biogenic origin
1000 for Earth's oldest putative microfossils. *Geology*, **37**, 631-634.
1001
1002 Donoghue, P.C.J., Bengtson, S., Dong, X., Gostling, N.J., Hultgren, T., Cunningham, J.A.,
1003 Yin, C., Yue, Z., Peng, F. & Stampanoni, M. 2006. Synchrotron X-ray tomographic
1004 microscopy of fossil embryos. *Nature*, **442**, 680-683.
1005
1006 Dutta, S., Hartkopf-Froder, C., Witte, K., Brocke, R. & Mann, U. 2013. Molecular
1007 characterization of fossil palynomorphs by transmission micro-FTIR spectroscopy:
1008 Implications for hydrocarbon source evaluation. *International Journal of Coal Geology*, **115**,
1009 13-23.
1010
1011 Edwards, N.P., Manning, P.L., Bergmann, U., Larson, P.L., van Dongen, B.E., Sellers, W.I.,
1012 Webb, S.M., Sokaras, D., Alonso-Mori, R., Ignatyev, K. & Barden, H.E. 2014. Leaf
1013 metallome preserved over 50 million years. *Metallomics*, **6**, 774-782.
1014
1015 Farquhar, J., Cliff, J., Zerkle, A.L., Kamyshny, A., Poulton, S.W., Claire, M., Adams, D. &
1016 Harms, B. 2013. Pathways for Neoproterozoic pyrite formation constrained by mass-independent
1017 sulfur isotopes. *Proceedings of the National Academy of Sciences USA*, **110**, 17638-17643.
1018
1019 Fenter, P., Rivers, M., Sturchio, N., Sutton, S. (Eds.) 2002. *Applications of Synchrotron*
1020 *Radiation in Low-Temperature Geochemistry and Environmental Sciences*. Reviews in
1021 Mineralogy and Geochemistry, Volume 49, Mineralogy Society of America, Washington
1022 DC.
1023
1024 Foucher, F. & Westall, F. 2013. Raman imaging of metastable opal in carbonaceous
1025 microfossils of the 700–800Ma Old Draken Formation. *Astrobiology*, **13**, 57-67.

- 1026 Fries, M. & Steele, A. 2011. Raman spectroscopy and confocal Raman imaging in
1027 mineralogy and petrography. *Springer series in Optical Sciences*, **158**, 111-135.
1028
- 1029 Garwood, R.J. & Dunlop, J. 2014. The walking dead: Blender as a tool for paleontologists
1030 with a case study on extinct arachnids. *Journal of Paleontology*, **88**, 735-746.
1031
- 1032 Garwood, R.J. & Sutton, M.D. 2010. X-ray micro-tomography of Carboniferous stem-
1033 Dictyoptera: new insights into early insects. *Biology Letters*, **6**, 699-702.
1034
- 1035 Garwood, R.J., Ross, A., Sotty, D., Chabard, D., Charbonnier, S., Sutton, M. & Withers, P.J.
1036 2012. Tomographic reconstruction of neopterous Carboniferous insect nymphs. *PLoS one*, **7**,
1037 e45779.
1038
- 1039 Grey, K. 1999. A modified palynological preparation technique for the extraction of large
1040 Neoproterozoic acanthomorph acritarchs and other acid insoluble microfossils. Geological
1041 Survey of Western Australia, Record 1999/10.
1042
- 1043 Hagadorn, J.W., Xiao, S., Donoghue, P.C.J., Bengtson, S., Gostling, N.J., Pawlowska, M.,
1044 Raff, E.C., Raff, R.A., Turner, F.R., Chongyu, Y., Zhou, C., Yuan, X., McFeely, M.B.,
1045 Stampanoni, M. & Neilson, K.H. 2006. Cellular and subcellular structure of Neoproterozoic
1046 animal embryos. *Science*, **314**, 291-294.
1047
- 1048 Halbhuer, K.-J. & Konig, K. 2003. Modern laser scanning microscopy in biology,
1049 biotechnology and medicine. *Annals of Anatomy*, **185**, 1-20.
1050
- 1051 Haubitz, B., Prokop, M., Doehring, W., Ostrom, J.H. & Wellnhofer, P. 1988. Computed
1052 tomography of *Archaeopteryx*. *Palaeobiology*, **14**, 206-213.
1053
- 1054 Hickman Lewis, K., Garwood, R., Withers, P. & Wacey, D. 2016. Using X-ray CT to inform
1055 on the petrological context of Precambrian cellular remains. *Journal of the Geological*
1056 *Society London* (this volume).
1057
- 1058 Hofmann, H.J. 1976. Precambrian microflora, Belcher Islands, Canada: Significance and
1059 systematics. *Journal of Palaeontology*, **50**, 1040-1073.
1060
- 1061 House, C.H., Schopf, J.W., McKeegan, K.D., Coath, C.D., Harrison, T.M. & Stetter, K.O.
1062 2000. Carbon isotopic composition of individual Precambrian microfossils. *Geology*, **28**,
1063 707-710.
1064
- 1065 Huldtgren, T., Cunningham, J.A., Yin, C., Stampanoni, M., Marone, F., Donoghue, P.C.J. &
1066 Bengtson, S. 2011. Fossilized nuclei and germination structures identify Ediacaran “animal
1067 embryos’ as encysting protists. *Science*, **334**, 1696-1699.
1068
- 1069 Igisu, M., Ueno, Y., Shimojima, M., Nakashima, S., Awramik, S.M., Ohta, H., & Maruyama,
1070 S. 2009. Micro-FTIR spectroscopic signatures of bacterial lipids in Proterozoic microfossils.
1071 *Precambrian Research*, **173**, 19-26.
1072
- 1073 Igisu, M., Takai, K., Ueno, Y., Nishizawa, M., Nunoura, T., Hirai, M., Kaneko, M., Naraoka,
1074 H., Shimojima, M., Hori, K., Nakashima, S., Ohta, H., Maruyama, S. & Isozaki, Y. 2012.
1075 Domain-level identification and quantification of relative prokaryote cell abundance in

1076 microbial communities by micro-FTIR spectroscopy. *Environmental Microbiology Reports*,
1077 4, 42-49.
1078
1079 Ireland, T.R. 1995. Ion microprobe mass spectrometry: techniques and applications in
1080 cosmochemistry, geochemistry, and geochronology. In: *Advances in Analytical Geochemistry*
1081 (eds Hyman M, Rowe M). JAI Press, Greenwich, CT, pp. 1-118.
1082
1083 Javaux, E.J., Knoll, A.H. & Walter, M.R. 2004. TEM evidence for eukaryotic diversity in
1084 mid-Proterozoic oceans. *Geobiology*, 2, 121-132.
1085
1086 Jehlicka, J., Urban, O. & Pokorny, J. 2003. Raman spectroscopy of carbon and solid
1087 bitumens in sedimentary and metamorphic rocks. *Spectrochimica Acta A*, 59, 2341-2352.
1088
1089 **Kak, A.C. & Slaney, M. 2001. *Principles of Computerized Tomographic Imaging*. Society of**
1090 **Industrial and Applied Mathematics, Philadelphia.**
1091
1092 Kempe, A., Wirth, R., Altermann, W., Stark, R.W., Schopf, J.W. & Heckl, W.M. 2005.
1093 Focussed ion beam preparation and in situ nanoscopic study of Precambrian acritarchs.
1094 *Precambrian Research*, 140, 36-54.
1095
1096 Kilburn, M.R. & Wacey, D. 2015. NanoSIMS as an analytical tool in the geosciences. In:
1097 Grice, K. (Ed.). *Principles and Practice of Analytical Techniques in Geosciences*. The Royal
1098 Society of Chemistry, Oxfordshire, UK. ISBN: 978-18-497-3649-7, pp. 1-34.
1099
1100 Knoll, A.H. 1994. Proterozoic and Early Cambrian protists: Evidence for accelerating
1101 evolutionary tempo. *Proceedings of the National Academy of Sciences USA*, 91, 6743-6750.
1102
1103 Knoll, A.H. 2015. *Life on a Young Planet: The First Three Billion Years of Evolution on*
1104 *Earth* (2nd Edition). Princeton University Press, 296p.
1105
1106 Knoll, A.H., Javaux, E.J., Hewitt, D. & Cohen, P. 2006. Eukaryotic organisms in Proterozoic
1107 oceans. *Philosophical Transactions of the Royal Society B*, 361, 1023-1038.
1108
1109 **Lawrence, J.R., Swerhone, G.D.W., Leppard, G.G., Araki, T., Zhang, X., West, M.M. &**
1110 **Hitchcock, A.P. 2003. Scanning transmission X-ray, laser scanning, and transmission**
1111 **electron microscopy mapping of the exopolymeric matrix of microbial biofilms. *Applied and***
1112 ***Environmental Microbiology*, 69, 5543-5554.**
1113
1114 Lemelle, L., Labrot, P., Salome, M., Simionovici, A., Viso, M. & Westall, F. 2008. In situ
1115 imaging of organic sulfur in 700-800 My-old Neoproterozoic microfossils using X-ray
1116 spectromicroscopy at the S K-edge. *Organic Geochemistry*, 39, 188-202.
1117
1118 Limaye, A. 2012. Drishti: a volume exploration and presentation tool. In: *SPIE Optical*
1119 *Engineering+ Applications* (pp. 85060X-85060X). International Society for Optics and
1120 Photonics.
1121
1122 Marshall, C.P. & Olcott Marshall, A, 2013. Raman hyperspectral imaging of microfossils:
1123 potential pitfalls. *Astrobiology*, 13, 920-931.
1124

- 1125 Marshall, C.P., Javaux, E.J., Knoll, A.H. & Walter, M.R. 2005. Combined micro-Fourier
1126 transform infrared (FTIR) spectroscopy and micro-Raman spectroscopy of Proterozoic
1127 acritarchs: A new approach to palaeobiology. *Precambrian Research*, **138**, 208-224.
1128
- 1129 Marshall, C.P., Emry, J.R. & Olcott Marshall, A. 2011. Haematite pseudomicrofossils present
1130 in the 3.5-billion-year-old Apex Chert. *Nature Geoscience*, **4**, 240-243.
1131
- 1132 Mayo, D.W., Miller, F.A., & Hannah, R.W. (Eds.). 2004. *Course Notes on the Interpretation*
1133 *of Infrared and Raman Spectra*. Wiley Online Library, Hoboken, NJ.
1134
- 1135 McCollom, T.M. & Seewald, J.S. 2006. Carbon isotope composition of organic compounds
1136 produced by abiotic synthesis under hydrothermal conditions. *Earth and Planetary Science*
1137 *Letters*, **243**, 64-84.
1138
- 1139 Moczydlowska, M. & Willman, S. 2009. Ultrastructure of cell walls in ancient microfossils
1140 as a proxy to their biological affinities. *Precambrian Research*, **173**, 27-38.
1141
- 1142 Moreau, J.W. & Sharp, T.G. 2004. A transmission electron microscopy study of silica and
1143 kerogen biosignatures in ~1.9 Ga Gunflint microfossils. *Astrobiology*, **4**, 196-210.
1144
- 1145 Oehler, D.Z. 1977. Pyrenoid-like structures in Late Precambrian algae from the Bitter
1146 Springs Formation. *Journal of Paleontology*, **51**, 885-901.
1147
- 1148 Oehler, D.Z., Robert, F., Mostefaoui, S., Meibom, A., Selo, M. & McKay, D.S. 2006.
1149 Chemical mapping of Proterozoic organic matter at submicron spatial resolution.
1150 *Astrobiology*, **6**, 838-850.
1151
- 1152 Oehler D.Z., Robert, F., Walter, M.R., Sugitani, K., Allwood, A., Meibom, A., Mostefaoui,
1153 S., Selo, M., Thomen, A. & Gibson, E.K. 2009. NanoSIMS: Insights to biogenicity and
1154 syngeneity of Archaean carbonaceous structures. *Precambrian Research*, **173**, 70-78.
1155
- 1156 Pacton, M., Fiet, N. & Gorin, G. 2007. Bacterial activity and preservation of sedimentary
1157 organic matter: the role of exopolymeric substances. *Geomicrobiology Journal*, **24**, 571-581.
1158
- 1159 Pang, K., Tang, Q., Schiffbauer, J.D., Yao, J., Yuan, X., Wan, B., Chen, L., Ou, Z. & Xiao,
1160 S. 2013. The nature and origin of nucleus-like intracellular inclusions in Paeoproterozoic
1161 eukaryote microfossils. *Geobiology*, **11**, 499-510.
1162
- 1163 Parnell, J., Brasier, M., Wacey, D., Bowden, S., Spinks, S., Boyce, A.J., Davidheiser-Kroll,
1164 B., Jeon, H. & Kilburn, M.R. 2016. **Contrasting microfossil preservation between two**
1165 **Torridonian lakes and implications for the fossil record.** *Journal of the Geological Society*
1166 *London* (this volume).
1167 .
- 1168 Pasteris, J.D. & Wopenka, B. 2003. Necessary, but not sufficient: Raman identification of
1169 disordered carbon as a signature of ancient life. *Astrobiology*, **3**, 727-738.
1170
- 1171 Qu, Y., Engdahl, A., Zhu, S., Vajda, V. & McLoughlin, N. 2015. Ultrastructural
1172 heterogeneity of carbonaceous material in ancient cherts: Investigating biosignature origin
1173 and preservation. *Astrobiology*, **15**, 825-842.
1174

1175 Rahman, I.A. & Zamora, S. 2009. The oldest cinctan carpod (stem-group Echinodermata),
1176 and the evolution of the water vascular system. *Zoological Journal of the Linnean Society*,
1177 **157**, 420-432.
1178
1179 Rasmussen, B. 2000. Filamentous microfossils in a 3,235-million-year-old volcanogenic
1180 massive sulphide deposit. *Nature*, **405**, 676-679.
1181
1182 Rasmussen, B., Fletcher, I.R., Brocks, J.J. & Kilburn, M.R. 2008. Reassessing the first
1183 appearance of eukaryotes and cyanobacteria. *Nature*, **455**, 1101-1104.
1184
1185 Rasmussen, B., Blake, T.S., Fletcher, I.R. & Kilburn, M.R. 2009. Evidence for microbial life
1186 in syngedimentary cavities from 2.75 Ga terrestrial environments. *Geology*, **37**, 423-426.
1187
1188 Rowe, T.B., Colbert, M., Ketcham, R.A., Maisano, J. & Owen, P. 2001. High-resolution X-
1189 ray computed tomography in vertebrate morphology. *Journal of Morphology*, **248**, 277-278.
1190
1191 Schiffbauer, J.D. & Xiao, S. 2009. Novel application of focused ion beam electron
1192 microscopy (FIB-EM) in preparation and analysis of microfossil ultrastructures: A new view
1193 of complexity in early eukaryotic organisms. *Palaios*, **24**, 616-626.
1194
1195 Schiffbauer, J.D., Xiao, S., Sharma, K.S. & Wang, G. 2012. The origin of intracellular
1196 structures in Ediacaran metazoan embryos. *Geology*, **40**, 223-226.
1197
1198 Schopf, J.W. & Kudryavtsev, A.B. 2005. Three-dimensional Raman imagery of Precambrian
1199 microscopic organisms. *Geobiology*, **3**, 1-12.
1200
1201 Schopf, J.W. & Kudryavtsev, A.B. 2009. Confocal laser scanning microscopy and Raman
1202 imaging of ancient microscopic fossils. *Precambrian Research*, **173**, 39-49.
1203
1204 Schopf, J.W., Kudryavtsev, A.B., Agresti, D.G., Czaja, A.D. & Wdowiak, T.J. 2005. Raman
1205 imagery: A new approach to assess the geochemical maturity and biogenicity of
1206 permineralized Precambrian fossils. *Astrobiology*, **5**, 333-371.
1207
1208 Schopf, J.W., Tripathi, A.B. & Kudryavtsev, A.B. 2006. Three-dimensional confocal optical
1209 imagery of Precambrian microscopic organisms. *Astrobiology*, **6**, 1-16.
1210
1211 Schopf, J.W., Tewari, V.C. & Kudryavtsev, A.B. 2008. Discovery of a new chert-
1212 permineralized microbiota in the Proterozoic Buxa Formation of the Ranjit Window, Sikkim,
1213 Northeast India, and its astrobiological implications. *Astrobiology*, **8**, 735-746.
1214
1215 She, Z., Strother, P., McMahon, G., Nittler, L.R., Wang, J., Zhang, J., Sang, L., Ma, C. &
1216 Papineau, D. 2013. Terminal Proterozoic cyanobacterial blooms and phosphogenesis
1217 documented by the Doushantuo granular phosphorites I: In situ micro-analysis of textures
1218 and composition. *Precambrian Research*, **235**, 20-35.
1219
1220 Spencer, A.R.T., Hilton, J. & Sutton, M.D. 2013. Combined methodologies for three-
1221 dimensional reconstruction of fossil plants preserved in siderite nodules: *Stephanospermum*
1222 *braidwoodensis* nov sp (Medullosales) from the Mazon Creek lagerstatte. *Review of*
1223 *Palaeobotany and Palynology*, **188**, 1-17.
1224

1225 Stern, R.A., Bodorkos, S., Kamo, S.L., Hickman, A.H., & Corfu, F. 2009. Measurement of
1226 SIMS instrumental mass fractionation of Pb isotopes during zircon dating. *Geostandards and*
1227 *Geoanalytical Research*, **33**, 145-168.
1228
1229 Stewart, A.D. & Parker, A. 1979. Palaeosalinity and environmental interpretation of red beds
1230 from the Late Precambrian ('Torridonian') of Scotland. *Sedimentary Geology*, **22**, 229-241.
1231
1232 Strother, P.K., Battison, L., Brasier, M.D. & Wellman, C.H. 2011. Earth's earliest non-
1233 marine eukaryotes. *Nature*, **473**, 505-509.
1234
1235 Streng M., Butler A.D., Peel J.S., Garwood R.J. & Caron J. 2016. A new family of Cambrian
1236 rhynchonelliformean brachiopods (Order Naukatida) with an aberrant coral-like morphology.
1237 *Palaeontology*, in press.
1238
1239 Strother, P.K. & Wellman, C.H. 2015. Palaeoecology of a billion-year-old non-marine
1240 cyanobacterium from the Torridon Group and Nonsuch Formation. *Palaeontology*
1241 doi:10.1111/pala.12212.
1242
1243 Sutton, M.D. 2008. Tomographic techniques for the study of exceptionally preserved fossils.
1244 *Proceedings of the Royal Society B*, **275**, 1587-1593.
1245
1246 Sutton, M.D., Briggs, D.E.G., Siveter, D.J. & Siveter, D.J. 2001. An exceptionally preserved
1247 vermiform mollusk from the Silurian of England. *Nature*, **410**, 461-463.
1248
1249 Sutton, M.D., Garwood, R.J., Siveter, D.J. & Siveter, D.J. 2012. SPIERS and VAXML: A
1250 software toolkit for tomographic visualization and a format for virtual specimen interchange.
1251 *Palaeontologica Electronica*, 15(2):5T.
1252
1253 Sutton, M.D., Rahman, I.A. & Garwood, R.J. 2014. *Techniques for Virtual Palaeontology*.
1254 Wiley Blackwell, 208p.
1255
1256 Thomen, A., Robert, F. & Remusat, L. 2014. Determination of the nitrogen abundance in
1257 organic materials by NanoSIMS quantitative imaging. *Journal of Analytical Atomic*
1258 *Spectrometry*, **29**, 512.
1259
1260 Templeton, A. & Knowles, E. 2009. Microbial transformations of minerals and metals:
1261 Recent advances in geomicrobiology derived from synchrotron-based x-ray spectroscopy and
1262 x-ray microscopy. *Annual Reviews in Earth and Planetary Science*, **37**, 367-391.
1263
1264 Tice, M.M, Bostick, B.C. & Lowe, D.R. 2004. Thermal history of the 3.5-3.2 Ga Onverwacht
1265 and Fig Tree Groups, Barberton greenstone belt, South Africa, inferred by Raman
1266 microspectroscopy of carbonaceous material. *Geology*, **32**, 37-40.
1267
1268 Vandenbroucke, M. & Largeau, C. 2007. Kerogen origin, evolution and structure. *Organic*
1269 *Geochemistry*, **38**, 719-833.
1270
1271 Wacey, D. 2014. In situ morphologic, elemental and isotopic analysis of Archean life. In:
1272 Dilek, Y. & Furnes, H. (Eds.) *Evolution of Archean Crust and Early Life*. Modern
1273 Approaches in Solid Earth Sciences, **7**, pp. 351-365, Springer.
1274

1275 Wacey, D., Kilburn, M.R., Saunders, M., Cliff, J., Brasier, M.D. 2011. Microfossils of sulfur
1276 metabolizing cells in ~3.4 billion year old rocks of Western Australia. *Nature Geoscience*, **4**,
1277 698-702.
1278
1279 Wacey, D., Menon, S., Green, L., Gerstmann, D., Kong, C., McLoughlin, N., Saunders, M. &
1280 Brasier, M.D. 2012. Taphonomy of very ancient microfossils from the ~3400 Ma Strelley
1281 Pool Formation and ~1900 Ma Gunflint Formation: new insights using focused ion beam.
1282 *Precambrian Research*, **220-221**, 234-250.
1283
1284 Wacey, D., McLoughlin, N., Kilburn, M.R., Saunders, M., Cliff, J., Kong, C., Barley, M.E. &
1285 Brasier, M.D. 2013. Nano-scale analysis reveals differential heterotrophic consumption in the
1286 ~1.9 Ga Gunflint Chert. *Proceedings of the National Academy of Sciences USA*, **110**, 8020-
1287 8024.
1288
1289 Wacey, D., Saunders, M., Roberts, M., Menon, S., Green, L., Kong, C., Culwick, T.,
1290 Strother, P. & Brasier, M.D. 2014. Enhanced cellular preservation by clay minerals in 1
1291 billion-year-old lakes. *Nature Scientific Reports*, **4**, 5841; DOI:10.1038/srep05841.
1292
1293 Westall, F., de Ronde, C.E.J., Southam, G., Grassineau, N., Colas, M., Cockell, C. &
1294 Lammer, H. 2006. Implications of a 3.472-3.333 Gyr-old subaerial microbial mat from the
1295 Barberton greenstone belt, South Africa for the UV environmental conditions on the early
1296 Earth. *Philosophical Transactions of the Royal Society B*, **361**, 1857-1875.
1297
1298 Williams, D.B. & Carter, C.B. 2009. *Transmission Electron Microscopy: A Textbook for*
1299 *Materials Science* (2nd edition). Springer Science and Business Media, New York, 832p.
1300
1301 Williford, K.H., Ushikubo, T., Schopf, J.W., Lepot, K., Kitajima, K. & Valley, J.W. 2013.
1302 Preservation and detection of microstructural and taxonomic correlations in the carbon
1303 isotopic compositions of individual Precambrian microfossils. *Geochimica et Cosmochimica*
1304 *Acta*, **104**, 165-182.
1305
1306 Wirth, R. 2009. Focused Ion Beam (FIB) combined with SEM and TEM: Advanced
1307 analytical tools for studies of chemical composition, microstructure and crystal structure in
1308 geomaterials on a nanometre scale. *Chemical Geology*, **261**, 217-229.
1309
1310 Wopenka, B. & Pasteris, J.D. 1993. Structural characterization of kerogens to granulite-facies
1311 graphite: Applicability of Raman microprobe spectroscopy. *American Mineralogist*, **78**, 533-
1312 557.
1313
1314 Yin, L. & Li, Z. 1978. Precambrian microfloras of southwest China with reference to their
1315 stratigraphic significance. *Memoir Nanjing Institute of Geology and Palaeontology*,
1316 *Academia Sinica*, **10**, 41-108.
1317
1318 Young, R.J. & Moore, M.V. 2005. Dual-beam (FIB-SEM) systems. In: Gianuzzi & Stevie
1319 (Eds.) *Introduction to Focused Ion Beams. Instrumentation, Theory, Techniques and*
1320 *Practice*. Springer, pp. 246-268.
1321
1322

1323 **FIGURE CAPTIONS**

1324

1325 **Fig 1.** Optical microscopy of Torridonian microfossils, demonstrating common morphotypes
1326 present in the assemblage. **(a)** Highly degraded dark-walled vesicle. **(b)** Pristine dark-walled
1327 vesicle. **(c)** Light-walled vesicle, potentially possessing a double wall. **(d)** Cluster of light-
1328 walled spheroidal unicells, most with a dark spot indicating potential preservation of cell
1329 contents. **(e)** Cluster of light-walled cells with mutually adpressed cell walls. **(f)** Pair of
1330 spheroidal unicells with very prominent dark inner sphere. **(g)** Partially decomposed
1331 filamentous sheath. **(h)** Filamentous sheath with bulbous termination housing potential
1332 spheroidal cell. **(i)** Colony of light-walled elliptical cells comparable to *Eohalotheca*
1333 *lacustrina* described by Strother & Wellman (2015). **(j)** Pair of cells that may have divided
1334 **shortly before fossilisation**, each containing a dark spot. Scale bars are 20 µm for **(a-i)** and 10
1335 µm for **(j)**.

1336

1337 **Fig. 2.** Torridonian microfossils imaged and analysed by **SEM-SE**, coloured for easier
1338 interpretation. **(a)** Large, thick-walled vesicle, showing 'velvet-like' folds. **(b)** Smaller, thin-
1339 walled vesicles with a crinkled surface and finely irregular outline. **(c)** Vesicle with large
1340 hemispherical pits bounded by raised rims or 'collars'. **(d)** Subspherical rigid vesicle retaining
1341 a 3D structure, and bearing many irregular rounded holes. Pink coccoid structures attached to
1342 the vesicles in **(a-b)** are potential **fossil** heterotrophs (see also Fig. 3). Sample CAI-7,
1343 macerated from phosphate from Cailleach Head. All scale bars are 10 µm.

1344

1345 **Fig. 3.** Evidence of bacterial heterotrophy in SEM images. **(a-b)** **Rounded pits and occasional**
1346 **holes, irregularly distributed on the surface of larger vesicles' walls, (b) is enlargement of**
1347 **boxed area in (a). (c-d) Collapsed coccoid or bacillate cells ~5 µm across, occupying pits in**

1348 the walls of larger vesicles, occasionally with a thin raised lip, (d) is enlargement of boxed
1349 area in (c) with heterotrophs false coloured pink. (e) Densely packed colony of coccoid and
1350 bacillate cells (pink) continuous with amorphous degraded vesicular or EPS material (grey-
1351 green). (f) Higher magnification of colony in boxed area of (e), showing collapsed coccoid
1352 and bacillate structures arranged randomly with possible supporting and sheathing
1353 membrane. Sample CAI-7, macerated from phosphate from Cailleach Head. Scale bars are
1354 20 μm for (a, c, e) and 10 μm for (b, d, f).

1355

1356 **Fig. 4.** X-ray microtomography analysis of Torridonian rock chips. (a) Reconstruction of a
1357 CT scan of a rock chip using the *Nikon* instrument (voxels c. 5 μm), highlighting part of a
1358 phosphate nodule (purple) within a quartz-rich sediment (grey), plus a number of higher
1359 density grains that are likely pyrite or iron oxide (gold). (b) Reconstruction of an X-ray scan
1360 of a second rock chip using the Swiss Light Source Synchrotron (voxels 1.625 μm). This
1361 shows a mixture of phosphate and other denser phases rather evenly distributed through the
1362 rock chip with no distinct phosphate nodule. (c-d and f-g) Reconstruction of two putative
1363 vesicles identified in a higher resolution CT scan using the *Zeiss Xradia Versa* instrument
1364 (voxels c. 1.5 μm). The light micrograph images (e and h) show specimens observed in thin
1365 sections that may be analogous to those identified using CT. Scale bar is 2 mm for (a) 500
1366 μm for (b) and 20 μm for (c-h).

1367

1368 **Fig. 5.** Raman analysis of microfossils from the Torridonian Supergroup. (a) Optical
1369 photomicrograph of two coccoid microfossils from the Cailleach Head Formation, each
1370 containing dark interior spheroids (arrows). (b) Raman map of the carbon G $\sim 1600 \text{ cm}^{-1}$ peak
1371 showing that the microfossils have carbonaceous walls and the dark interior spheroids are
1372 also carbonaceous. This suggests that they are clumps of degraded cellular material or

1373 remnants of a cell nucleus. **(c)** Raman map of the major calcium phosphate (apatite) $\sim 960\text{ cm}^{-1}$
1374 peak showing that a large proportion of the mineralising phase is apatite. The patchy
1375 appearance of the apatite suggests the presence of further mineral phases, interpreted to be
1376 clay minerals as detected in higher resolution SEM and TEM analyses (see Figs 7-8). **(d)**
1377 Optical photomicrograph of a microfossil from the Stoer Group. Raman maps of the carbon
1378 G $\sim 1600\text{ cm}^{-1}$ peak **(e)**, pyrite $\sim 380\text{ cm}^{-1}$ peak **(f)**, calcite $\sim 1090\text{ cm}^{-1}$ peak **(g)**, and albite
1379 $\sim 510\text{ cm}^{-1}$ peak **(h)** demonstrating that the microfossil is partially pyritised but some
1380 carbonaceous composition remains, and that the sediment is dominantly calcite and feldspar.
1381 Scale bars are $10\text{ }\mu\text{m}$.

1382

1383 **Fig. 6.** NanoSIMS analysis of a microfossil from the Diabaig Formation. **(a)** Optical
1384 photomicrograph of a light-walled spheroidal cell with ruby red intracellular particles. **(b)**
1385 Overview of a FIB-milled wafer prepared for NanoSIMS from the region indicated by the
1386 yellow line in **(a)**. Note the contrast between the large dark-grey grains, which equate to the
1387 ruby red grains in **(a)**, and the remainder of the wafer, plus holes in the wafer likely induced
1388 by excessive FIB-milling. **(c)** NanoSIMS ion map of nitrogen measured as CN^- . **(d)**
1389 NanoSIMS ion map of sulfur measured as S^- . **(e)** NanoSIMS ion map of iron oxide measured
1390 as FeO^- . **(f)** Three colour overlay of nitrogen (blue), iron oxide (red) and silicon (green)
1391 showing that the large dark grains are iron oxides and they are located just inside the cell wall
1392 (intracellular). The other mineral phases are dominantly clays and quartz. Scale bar is $20\text{ }\mu\text{m}$
1393 in **(a)**, and $5\text{ }\mu\text{m}$ for **(b-f)**. Note scale bar in **(c)** also applies to **(d-f)**.

1394

1395 **Fig. 7.** TEM analysis of a FIB milled wafer extracted from a Torridonian microfossil. **(a)**
1396 Optical photomicrograph of a dark-walled spheroidal microfossil from the Cailleach Head
1397 Formation. **(b)** Overview of the FIB-milled wafer extracted from the region marked by the

1398 yellow line in (a) showing a complex wall structure and different mineral phases (indicated
1399 by different levels of grey within the image) inside and outside of the microfossil (from
1400 Wacey *et al.* 2014). (c) Three colour overlay of ChemiSTEM elemental maps of carbon
1401 (blue), aluminium (orange) and calcium (pink) from the region indicated by the dashed box in
1402 (b). Carbon represents the organic material of the microfossil walls, and at least four separate
1403 walls (or wall layers) can be seen. Calcium represents apatite, the dominant mineral phase
1404 outside of the microfossil. Aluminium represents clay minerals that infill the microfossil,
1405 occur between the walls of the microfossil and occur in minor amounts outside of the
1406 microfossil. Black areas are holes in the TEM wafer. Scale bar is 10 μm in (a), 2 μm in (b),
1407 and 1 μm in (c).

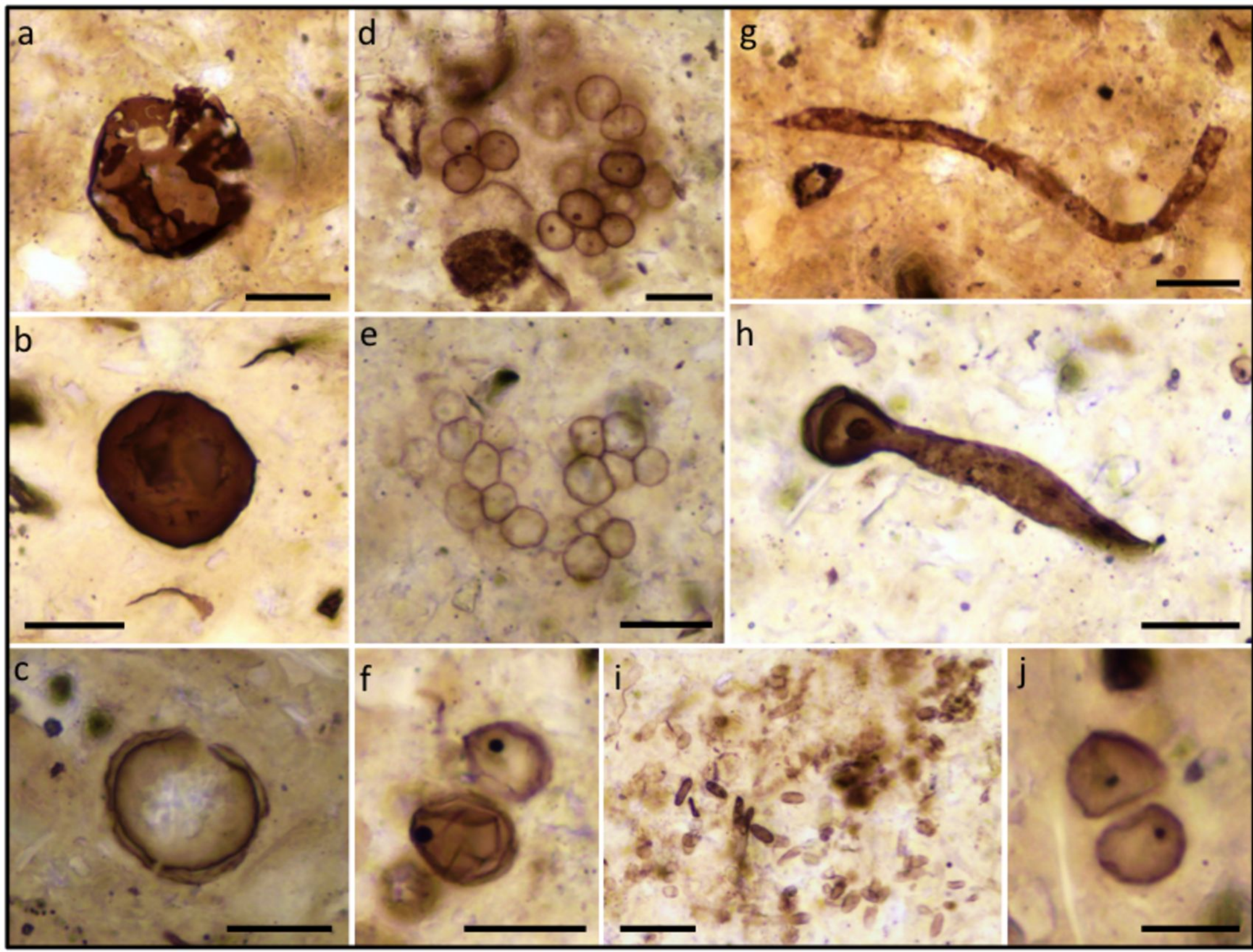
1408

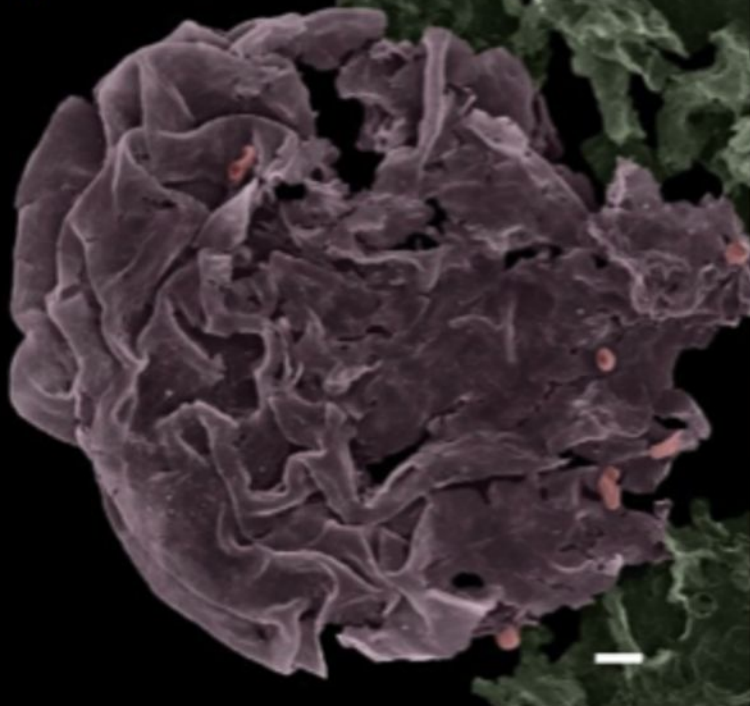
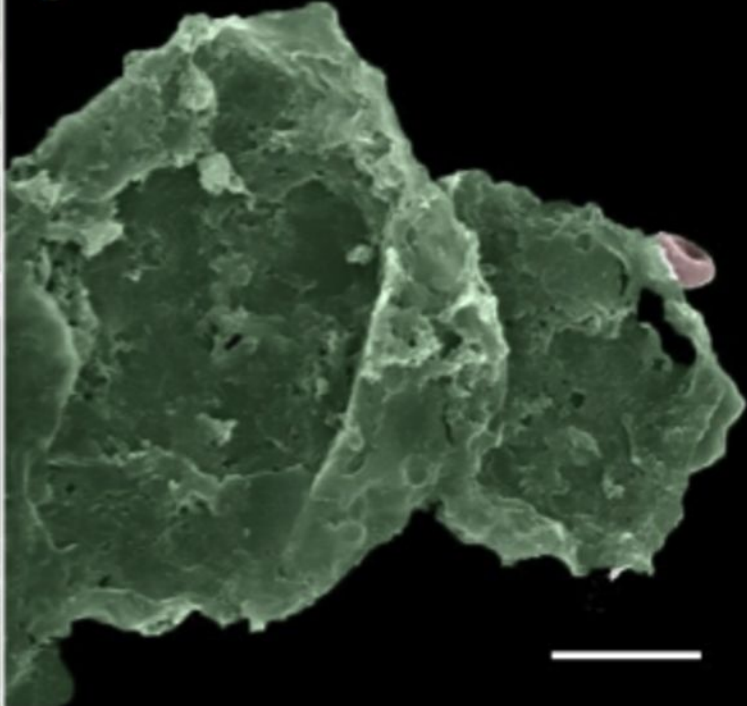
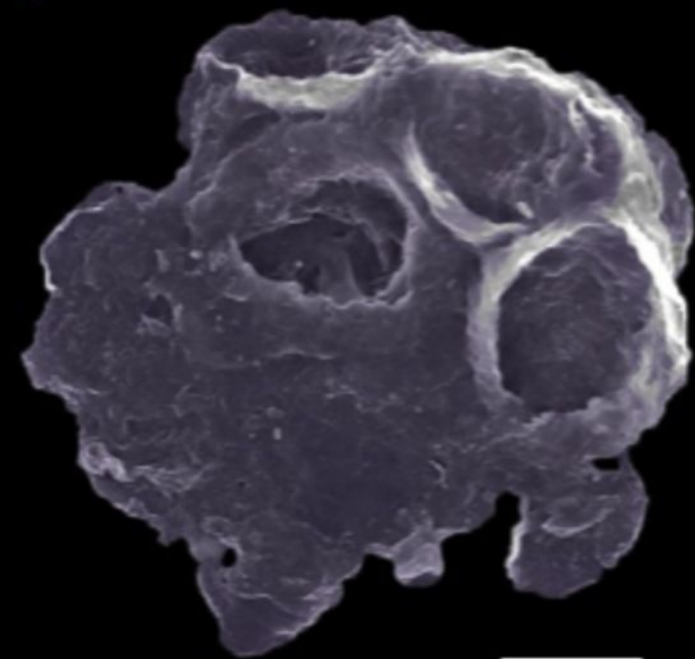
1409 **Fig. 8.** FIB-SEM-EDS of a microfossil from the Cailleach Head Formation. (a) Optical
1410 photomicrograph of a dark walled spheroidal vesicle showing the location of the FIB-milled
1411 area and direction of view for the other panels in the figure (from Wacey *et al.* 2014). (b)
1412 Secondary electron image showing the FIB-milled face below the surface of the thin section.
1413 Shown below are energy-dispersive X-ray (EDS) elemental maps of the FIB-milled face
1414 shown in (b). Carbon (light blue) represents the organic microfossil walls, highlighting a
1415 thick inner cyst wall and thinner outer vegetative cell wall. Phosphorus (red), calcium (pink)
1416 and moderate levels of oxygen (green) represent apatite, the dominant fossilising mineral
1417 outside of the microfossil. Iron (blue), plus moderate amounts of silicon (turquoise),
1418 aluminium (orange) and oxygen represents Fe-rich clay, occurring between the two
1419 microfossil walls, replacing parts of the outer wall, and continuing for 1–2 μm outside the
1420 outer wall. Potassium (yellow), plus silicon, aluminium and oxygen represents K-rich clay
1421 restricted to the interior of the vesicle.
1422 Scale bars are 5 μm .

1423

1424 **Fig. 9.** 3D FIB-SEM nano-tomography of a Torridon microfossil. **(a)** Optical
1425 photomicrograph of a cluster of light-walled spheroidal cells from the Cailleach Head
1426 Formation (from Wacey 2014). **(b)** Example of a FIB-milled slice through the cluster of
1427 microfossils in the region indicated by the dashed line in **(a)**. Note that portions of at least 8
1428 cells can be seen in this image, some of which are hidden from view below other cells in the
1429 optical photomicrograph. Note also dark material inside the upper central cell (dashed arrow)
1430 **(c-f)** 3D model of the cell indicated by the solid arrow in **(b)** viewed from four different
1431 orientations, showing the location of preserved cell contents (blue) with respect to the cell
1432 wall (yellow). Note that in (f) part of the cell wall has been removed to better visualize the
1433 cell contents. Scale bar is 10 μm in **(a)**, and 5 μm for **(b-f)**. Note scale bar in **(c)** also applies
1434 to **(d-f)**.

1435



a**b****c****d**

